Electronic Transport and Noise in Mesoscopic SNS/SFS-junctions

INAUGURALDISSERTATION
zur
Erlangung der Würde eines Doktors der Philosophie
vorgelegt der
Philosophisch-Naturwissenschaftlichen Fakultät
der Universität Basel
von

Tilman Hoss

aus Herrischried, Deutschland

Basel, 2000

Genehmigt von der Philosophisch-Naturwissenschaftlichen Fakultt
auf Antrag von:

Prof. Dr. C. Schönenberger
Prof. Dr. P. Martinoli
Prof. Dr. C. Bruder
Prof. Dr. C. Strunk

Basel, den 6. Juni 2000

Prof. Dr. Andreas D. Zuberbühler

Contents

Chapter 1

Introduction

In a macroscopic conductor electric transport appears as a continuous flow of charge. But when dimensions get small, i.e. small compared to the inelastic electron scattering length, a variety of new effects appear where the properties of the electron can be observed or even used for new electronic devices. In these so called *mesoscopic* dimensions, it is the behaviour of the electron as fermion with descrete charge e and its quantum mechanical behaviour as a propagating wave that is investigated. Of special interest is how charge transfer is supported or suppressed in different materials and how it can be manipulated. How do the electrons interact with each other or impurities? How do they react on confinement in two dimensions (2DEG), one (edge states, nanotubes) or even zero dimension (quantum dot). What are the effects of the quantum mechanical wave like behaviour? Where and how does the electrical transport take place in different materials like, metals, superconductors, polymers, carbon nanotubes or DNA? New technological achievments give access to so small dimensions of conductors that the particle and wave behavior of single electrons can be observed. On this small scale current can be controlled on a single electron level in quantum dots which will even be used as a new current standard. The granularity of the electrical current becomes apparent in the electronic noise. Since the current consists of single particles with descrete charge, the current exhibits characteristic fluctuations about its main value (shot noise). The Pauli exclusion principle for fermionic particles has an influence on the correlation between transmitted and reflected current at a semi transparent barrier (Hanbury, Brown and Twiss experiment for fermions). The superposition of the waves attributed to the electrons can be demonstrated in systems where the phase memory is maintained i.e. no inelastic scattering. In metallic rings where the phase of the partial waves can be tuned by a magnetic field the constructive or destructive superposition leads to oscillations in the conductance (Aharonov-Bohm rings).

In this thesis the electronic properties of normal metals (or ferromagnets) in contact to superconductors are studied with special focus on the mechanism that occurs when dissipative transport is transformed in dissipationless transport at the NS interface (Andreev Reflection). For the experiments the samples had to be small in two senses. First, short to observe effects related to the phase of the electrons which, in metals, is lost after a phase coherence length of the order of one micron. Second, narrow to have high resistances and hence good signal to noise ratio in the conductance and shot noise measurements. An additional requirement is a high purity of the metals and interfaces to keep scattering at impurities low. The samples where all measured in a cryostat at temperatures below the superconducting transition temperatures of niobium and aluminum. Low temperatures were also required for a long electron coherence length which grows as $1/T^{1/3}$. The range of the proximity effect, an induced superconductivity in the normal metal, increases as $L_T \propto 1/T^{1/2}$.

A new fabrication technique was developed to produce submicron hybrid structures. The attempt to circumvent the ordinarily used lift off technique with an organic resist was motivated by the low thermal stability of these polymeres [1]. To achieve a high purity of the deposited metals a mask was needed which causes no contamination. Our nonorganic evaporation mask proved to be very effective especially for high melting materials (i.e. Nb). In addition it is very well suited for angle evaporation in high or even ultrahigh vacuum systems. With this technique very clean contacts between superconductor normal metal and ferromagnet were realised which is essential for the mechanism of Andreev reflection studied in this thesis.

This thesis is divided into four major parts. An introductory part to mesoscopic physics (chap.2) a part about our new fabrication technique of submicron size samples and tests which emphasize the advantages of this procedure (chap.3,5), a part describing the cryostat and the measurement setup (chap.4). In the last part (chap.6,7) the experiments on electrical transport and noise in SNS and SFS hybrid structures are presented.

Chapter 2

Mesoscopic systems

2.1 Electrical transport and shot noise in mesoscopic systems

In mesoscopic physics a now well established description of electrical transport as a scattering problem was first developed by Landauer [2]. In his picture transport is a result of carrier flow incident on the sample boundaries with a Fermi energy distribution of the reservoirs. The voltage drop is a consequence of scattering of the electrons in the sample and an accumulation of charge carriers. In other words the conductance is related to the quantum mechanical transmission of electrons through the sample.

For a narrow conductor of a width smaller than the fermi wave length, the lateral constriction allows only one transmission mode. If the chemical potential μ_1 on the left side is higher than μ_2 on the right side, the electrons of states in the range between μ_1 and μ_2 will flow from the left to the right. The current will be [3],

$$j = -(\mu_1 - \mu_2)ev(dn/d\mu) \tag{2.1}$$

with v along the transport axis at the Fermi surface and $dn/d\mu = 1/\pi\hbar v$ the density of states in one dimension. With $\mu_1 - \mu_2 = -eU$ and U the applied voltage the resulting conductance is,

$$G = \frac{j}{U} = \frac{e^2}{\pi\hbar} \tag{2.2}$$

This result has been confirmed experimentally in quantum point contacts. If there is an obstacle in the channel, which transmits with probability Θ, the conductance will be reduced to,

$$G = \frac{e^2}{\pi\hbar}\Theta \tag{2.3}$$

This formalism has been generalized to multiple modes transport and can be used for diffusive wires too.

That electrical current is carried by transport channels of discrete conductance with a transmission probablity ranging from 0 to 1 is at the origin of electronic noise. Electronic noise S_I is the deviation of the current from its average value and is produced when electrons are scattered from occupied to empty states with a certain probability. The entity that is measured in noise experiments is the mean square current fluctuation per frequency bandwidth.

$$S_I(\omega) := \left\langle (\Delta I_{band})^2 \right\rangle / \Delta f \tag{2.4}$$

The uncertainty of whether an electron is transmitted or not gives rise to current fluctuations, proportional to $\Theta(1-\Theta)$. The noise at zero temperature is given by [4]:

$$S_I = 2e\left|V\right| \frac{e^2}{h} \sum_{n=1}^{N} \Theta_n \left(1-\Theta_n\right) \tag{2.5}$$

where Θ_n is the transmission probability of channel n and N the number of occupied channels.

The current in completely open channels ($\Theta = 1$) and completely closed ($\Theta = 0$) is not fluctuating and hence is not contributing to the noise. For example in a tunnel junction with transport modes of low transmission the current fluctuations are maximum and proportional to the electrical charge and the current [5].

$$S_I = 2eI \qquad \text{(full shot noise or Poisson noise)} \tag{2.6}$$

Shot noise may be interpreted as an indication that the transport mechanism through the structure involves discrete transfer of charge, as opposed to the continuous charge transfer that takes place in macroscopic conductors. On the other hand, in equilibrium the electrons will have a fermi distribution which is given by the bath temperature. The noise is proportional to the broadening of the fermi distribution f (Johnson Nyquist noise [6]), hence the temperature T.

$$S_I = \frac{4k_BT}{R} \qquad \text{(thermal noise for } eV = 0\text{)} \tag{2.7}$$

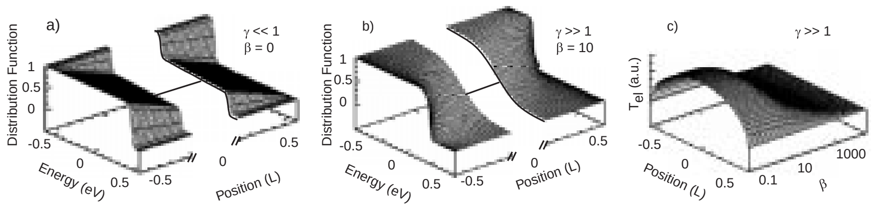

Figure 2.1: from ref. [8] a) electron distribution function without scattering ($\beta = L/l_{e-ph}$, $\gamma = L/l_{e-e}$). b) for e-e scattering. c) electron temperature profile in dependence on the electron-phonon interaction parameter β for strong e-e scattering.

Excess or shot noise can be observed in a driven system with a nonequilibrium electron distribution, like in wires which are shorter than the electron phonon relaxation length L_{e-ph}. In this out-of-equilibrium regime, noise is proportional to the current going through the conductor. A quantum supression of the full shot noise appears in conductors shorter than the electron-electron scattering length. It has been shown by random matrix theory [7] that the distribution of the transmission probabilities is peaked at 0 and 1. This means that most channels are noiseless and the Poissonian noise is reduced by a factor of 1/3:

$$S_I = \frac{1}{3} 2eI \qquad\qquad (L << l_{e-e}) \tag{2.8}$$

To include inelastic scattering Nagaev developed a semiclassical formalism which derives noise as a fluctuation in the electron state occupation number given by $f(1-f)$. These fluctuations are energy dependent and the total noise is obtained by averaging over the whole wire:

$$S_I = 4G \left\langle \int_{-\infty}^{\infty} f(E,x)\left[1 - f(E,x)\right] dE \right\rangle_{wire} \tag{2.9}$$

for electron-electron scattering the following equation was derived:

$$S_I = \frac{\sqrt{3}}{4} 2eI \qquad (l_{e-e} << L << l_{e-ph}) \tag{2.10}$$

The reduction factor with respect to full shot noise depends on whether the sample is shorter or longer than the electron-electron scattering length (l_{e-e}). In the case of $L << l_{e-e}$ the electrons diffuse from occupied to empty states without any energy exchange, which results in a two step distribution function (see fig 2.1 a). This gives rise to the 1/3 supression. In the case of e-e interaction the distribution function is the fermi distribution of the reservoirs at the ends and in the middle, where the coupling to the reservoirs is the weakest, the electrons have a broad energy distribution (see fig 2.1 b). The electron excess temperature (with respect to the phonon bath temperature) for strong e-e interaction is illustrated in fig 2.1 c) as a function of position and e-ph scattering. In the case of strong e-ph scattering (large β) there is no excess temperature and the profile is flat.

At finite temperatures and for small transmission coefficients Θ the crossover from thermal to shot noise is given by [9]

$$S_I = 2e\,|I|\coth\left(\frac{e\,|V|}{2kT}\right) \tag{2.11}$$

where in a driven system T can be higher than T_{bath}.

The equation 2.4 is called the spectral density and is often expressed by the fourier transform of the current correlation function.

$$S_I\,(\omega) = 2\int_{-\infty}^{\infty} \langle \Delta I\,(0)\,\Delta I\,(t)\rangle\, e^{iwt} dt \tag{2.12}$$

For uncorrelated transport we have

$$\langle \Delta I\,(0)\,\Delta I\,(t)\rangle = \langle \Delta I^2 \rangle e^{-t/\tau} \tag{2.13}$$

which is the mean square fluctuation with an exponential decay on the time scale of the correlation time τ. The correlation time is a measure of how sharp an event (i.e. electron transmission) is in time. This is in the order of nanoseconds. The integration gives

$$S_I(\omega) = \frac{2\langle \Delta I^2 \rangle 1/\tau}{(1/\tau)^2 + \omega^2} \tag{2.14}$$

Since $1/\tau$ is in the range of gigaherz the shot noise is frequency independent (white) for $\omega << 1/\tau$, where our measurements are done. This means that it is present also on long time scales and is not averaged out.

In some systems a frequency dependent noise can be superposed to the shot noise. When scatterers are present which have two stable positions, the scatterer can change from one to the other position by activation. Each time a scatterer changes its position the resistance and thus the current is also changed. An ensemble of such two level systems produces the so called $1/f$-noise [10] which is inverse proportional to the frequency and has a current dependency of $S_I \propto I^2$.

2.2 Mesoscopic superconductivity

In mesoscopic superconductivity one field of investigation is the change of the superconducting properties due to confinement in small geometries like in thin wires [11] or quantum dots [12]. Also the pairbreaking effects at magnetic impurities is of great interest [13]. Another important field is the influence of a superconductor in contact to a normal conductor via the proximity effect. The relevance of different length scales are examined, like the thermal diffusion lenght L_T, the phase coherence length L_φ or the length on which electron and hole pairs stay coherent L_{Th} which is related to the Thouless energy. The Josephson effect is studied extensively in different kinds of weak links where the connection between the superconductors can be a small constriction, a thin insulating layer, a normal metal or a ferromagnet. The ferromagnet should have a strong influence on the Andreev reflection since the spin bands are not equally occupied. The macroscopic phase of the Cooper pair condensate is of growing interest for quantum mechanical experiments like the quantum computing. The storage of magnetic flux quanta in superconducting rings is one candidate for a so called Q-bit [14].

2.2.1 Quasiparticle tunneling and Subgap current in NS

In the superconductor the electrons in the neighborhood of the Fermi surface experience an attractive potential and form electron pairs (Cooper pairs) of opposite spin and momentum. The consequence is a gap in the excitation spectrum around the Fermi energy (fig. 2.2). The density of states shows a singularity or at least a large maximum at the edge of the energy gap. The occupation of these excited states is governed by the Fermi distribution, the Cooper pairs are at the Fermi energy.

The gap can be observed in the I(V)-characteristic of a NS tunnel junction. For excitation energies smaller than the gap no single electron states are available in the superconductor and a tunneling current is suppressed. At large voltages electrons can tunnel into quasiparticle states above the gap which can be seen as a sharp onset of a current in I(V) (see fig.2.4). In the high voltage limit the I(V) aproaches the ohmic straight line. In the case of highly transparent NS contacts a second current transfer process appears, which was first described by Andereev [15]. This Andreev reflection (AR) is the dominant process at energies $E_k < \Delta$. Electrons reaching the interface from the normal side in the energy range of the gap are *retro*reflected as a hole into the normal part and travel the time reversed path. This is a two particle process transfering $2e$ across the interface and the probability

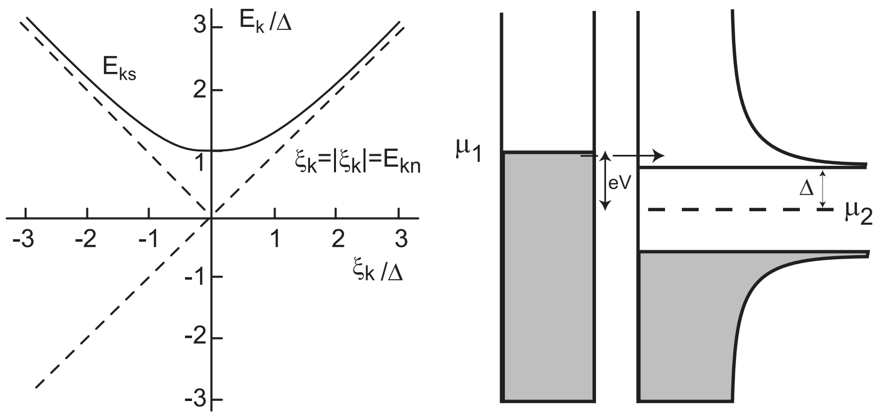

Figure 2.2: Energies of elementary excitations in the normal, E_{kn}, and the superconducting state, $E_{ks} = \left(\Delta^2 + \epsilon_k^2\right)^{1/2}$, as a function of energy difference to the Fermi level $\xi_N = |\epsilon_k - E_F|$. Right: density of states horizontally vs. energy in the normal and superconductor, shaded are the occupied states. Tunneling is only possible if empty states are available.

of transmission is Θ^2, which requires very clean interfaces.

Note that for the normal reflection only the components of velocity normal to the boundary change sign. In the case of AR all three components of the velocity are changing sign. This is because there are no excited states within the gap that could absorb this energy transfer. The incident electron at E_k is reflected as a hole of opposite spin at the same excitation energy E_{-k}. The two transmitted electrons decay into the Cooper pair condensate within a distance of the thermal diffusion length ξ_T. The Cooper pair consists of a spin up and a spin down electron at the Fermi energy. Andreev Reflection is thus an *elastic* scattering which means that no energy can be transferred via this process (see section 6.3).

Blonder, Tinkham and Klapwijk [16] calculated the current through a NS junction, separated by an insulating barrier:

$$I = (2e/h)\Omega \int_{-\infty}^{\infty} dE \left(f(E-eV) - f(E)\right)\left(1 + A(E) - B(E)\right) \tag{2.15}$$

where $A(E)$ and $B(E)$ are Andreev and normal reflection coefficients listed in table two of Blonder *et al*, $f(E)$ the fermi function and Ω a measure of the area of the junction. This expression leads to a subgap current as displayed in Fig (2.4).

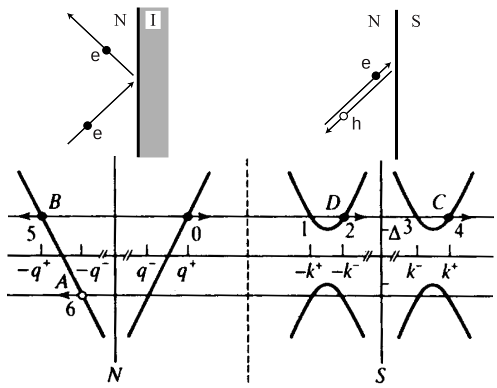

Figure 2.3: Top: Schematic of normal reflection at a barrier and AR at a transparent NS boundary. Bottom: energy vs. momentum on the two sides of an NS interface. The open circles denote holes; the closed circles, electrons; the arrows point in the direction of the group velocity, $\delta E_k/\delta k$. The schematic describes an electron at (0) the resulting transmitted (2,4) and the reflected (5,6) particles. A refers to Andreev-reflected hole and B to normal reflection.

2.2.2 Josephson current

The superconducting electrons can be described by the Ginzburg-Landau wave function Ψ and the local density of Cooper pairs is given by $n_S = |\Psi(x)|^2$. $\Psi(x) \equiv |\Psi(x)|\, e^{i\varphi(x)}$ is a many particle wave function and describes the Cooper pair condensate as a whole. The effect of the phase in the wave function was first pointed out by Josephson [17] who predicted a phase dependent tunneling current between superconductors at zero voltage difference of,

$$I = I_C sin(\varphi_1 - \varphi_2) \tag{2.16}$$

where I_C is the maximum critical current and φ_i the phase of the superconductors. This is the so called DC Josephson current. This effect is different from the tunneling discussed before. In a weak link there is an overlap of the superconducting order parameter from both sides and a certain density of Cooper pairs over the whole junction. Hence, phase coherent transfer of Cooper pairs is possible implying a supercurrent through the weak link. Josephson further predicted that if the critical current is exceeded and a voltage difference V is maintained across the junction the phase difference $\Delta\varphi$ will evolve according to,

$$\frac{\partial(\Delta\varphi)}{\partial t} = \frac{2eV}{\hbar} \tag{2.17}$$

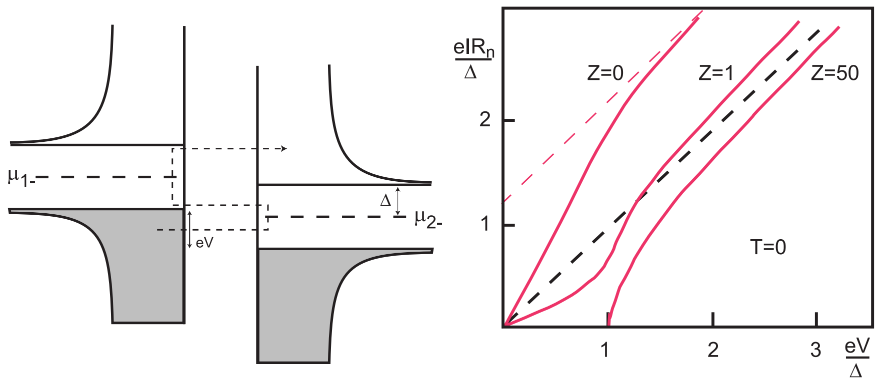

Figure 2.4: Left: The dashed line traces a representative trajectory through successive AR for a biase voltage $eV < 2\Delta$. Right: IV-characteristic for NS boundary with high barrier ($Z = 50$) and low barrier ($Z = 0$) [16]. The high transparency junction shows a subgap current in contrast to the high barrier junction. For higher voltages the I(V) for $Z = 50$ merges into a line which extrapolates through zero however for low Z the I(V) extrapolates to an offset current a zero biase voltage.

2.2.3 Josephson current in extended junctions

The phase sensitivity of the Josephson current manifests itself also in a single extended Josephson junction (JJ) penetrated by a flux Φ in the plane of the junction. The electrons passing the junction acquire an additional phase which is proportional to the flux inclosed in the junction cross section. The critical current in dependence of the magnetic field is then given by an expression which corresponds to the single slit interference in optics,

$$I_m = I_c \left| \frac{sin(\pi\Phi/\Phi_0)}{\pi\Phi/\Phi_0} \right| \tag{2.18}$$

where $\Phi_0 = h/2e = 2\text{mT}/\mu\text{m}^2$ is the flux quantum. If the sample is made of two parallel Josephson junctions (DC-squid) with an enclosed flux Φ between the junctions the maximum critical current is given by,

$$I_m = 2I_c \left| cos\pi\Phi/\Phi_0 \right| \tag{2.19}$$

This corresponds to the two slit experiment in optics (fig.2.5). The IV-characteristic of a JJ is displayed in fig 2.6. The current can be raised without a voltage drop until a critical point. There the junction jumps into the resistive state with an ohmic behaviour. The critical current for short

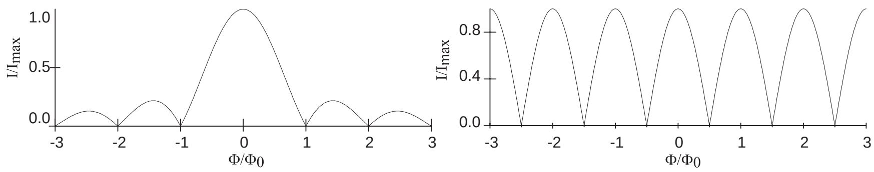

Figure 2.5: Fraunhofer pattern of the critical current as a function of magnetic field for an extended single junction (left) and two parallel junctions (right).

junctions can be calculated by the Ambegaokar-Baratoff formula:

$$I_c R_n = (\pi\Delta/2e)tanh(\Delta/2k_B T) \tag{2.20}$$

2.2.4 RSCJ-model

For most weak links at nonzero temperature a $finite$ resistance is observed below I_c. For junctions much shorter than the superconducting coherence length this effect can be explained with the resistively and capacitively shunted junction (RCSJ) model. In this model the phase difference between the superconductors is described as a particle moving in a tilted washboard potential where the slope is proportional to I/I_c and the height of the barrier is proportional to the Josephson coupling energy $E_J \equiv (\hbar I_c/2e)$ (see fig.2.6). For strong damping ($R_n C$ small) the phase difference $\Delta\varphi$ will follow the potential profile. When the junction is thermally activated the particle can overcome the barrier and $d\Delta\varphi/dt$ is nonzero which results in a voltage drop across the junction. Ambegaokar and Halperin calculated the IV-characteristic in dependence of the activation energy (fig.2.6)[18]. For T=0 it is given by $V = R\left(I^2 - I_c^2\right)^{1/2}$ which smoothly interpolates between $V = 0$ for $I < I_c$ and Ohm's law $V = RI$ for $I >> I_c$. When $k_B T$ is comparable to E_J (finite u in fig. 2.6) the system is rapidly jumping between trapped and running states, leading, on laboratory time scale of milliseconds, to a broadened resistive transition from a lowered I_{cT} to the ohmic behaviour.

2.2.5 Proximity effect

In our weak links the current consists of a "normal" component (quasiparticle tunneling, Andreev reflection) and a supercurrent which is due to the proximity effect. A superconductor can induce superconductivity into an attached normal metal or semiconductor. The strength of this effect is given by the superconducting order parameter pairing field (or pair amplitude) $F(x) = \langle\Psi_\uparrow(x)\Psi_\downarrow(x)\rangle$, which is related to the Ginzburg Landau order

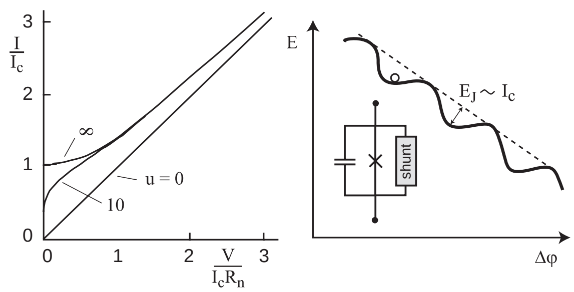

Figure 2.6: Left: Influence of phase slip on the IV characteristic for different $u = 2E_J/k_BT$ according to [18]. Right: schematic of tilted washboard potential of a resistively shunted JJ. Inset: JJ with capacitor and shunt resistor in paralell.

parameter. The pairing field decays exponentially as $F(x,\epsilon) \propto exp(-kx)$ with $k = \sqrt{\epsilon/\hbar D}$, and the corresponding critical current vanishes as $I_C \propto exp(\sqrt{L/L_T})$ where $L_T = \sqrt{\hbar D/2\pi k_B T}$ is the thermal diffusion length in N. With $\epsilon_T = \hbar D/L^2$ the condition for vanishing Josephson current is $\epsilon_T << k_BT$ or $L >> L_T$ respectively. ϵ_T is the Thouless energy and defines the energy range on which the electron-hole correlation is maintained over the whole sample length. The hole has the same excitation energy ϵ as the electron with respect to the Fermi energy. But it will have a change in wave vector $\delta k = \epsilon/\hbar v_F$ due to the branch crossing. After diffusion to a distance L this induces a phase shift $\delta\varphi = 2\pi\delta k v_F t_D = 2\pi\epsilon L^2/(\hbar D)$. Electron hole coherence is hence maintained in an energy window of $\epsilon_T = \hbar D/L^2$. Note that the pair potential $\Delta(x)$ vanishes in the normal metal so the proximity effect can be understood as a leakage of Cooper pairs into the normal metal. The proximity induced superconductivity is also very much dependent on the interface quality between the superconductor and the normal metal since the effect decays exponentially with the interface resistance. A variety of new phenomena can be seen in the energy range below the Thouless energy like the formation of a mini gap in the density of states in the normal metal [19], the reentrance of NS interfaces resistance to the normal state resistance [20] or long range coherence effects. It was shown that the fraction of electron-hole pairs with energies below ϵ_T contribute to quantum corrections of the conductance on distances much longer than L_T [21].

2.2.6 Andreev bound states

In SNS samples where the length of the N part is longer than L_T the Josephson supercurrent is suppressed. But if L is still shorter than the phase coherence length L_Φ a phase dependent current between the superconducting electrodes persists[22]. This effect is attributed to the formation of Andreev bound states between the superconducting boundaries. An Andreev cycle is created between two superconductors when an electron is Andreev reflected as a hole at on interface and again as an electron at the other interface. If the total phase acquired in one cycle equals $2\pi n$, where n is an integer, Andreev bound states are formed. The total phase change comprises the phase difference between the two superconductors $\Delta\Phi$ plus the quantum phases of the electrons and holes and a shift of $\pi/2$ per AR. This gives the condition: $k_e L - k_h L + \Delta\Phi + \pi = 2\pi n$. The energy dependence of a Andreev bound state, with respect to the Fermi level, is a periodic function of $\Delta\Phi$ and can be approximated by $\epsilon = \pm 3.1 E_T cos\Delta\Phi$ [23], where the sign refers to left and right going states respectively. Only the electrons below the Fermi energy contribute to the supercurrent while the states above the Fermi energy are empty. The current is then given by the slope of the occupied levels for given phase difference $\Delta\Phi$. At $\Delta\Phi = \pi$ a change in the direction of the supercurrent will occur. This effect can be explored in a SNS transistor where a "gate" current in N is used to tune the Fermi energy and by this means the occupation of the Andreev levels [24, 25]. In our experiments ϵ_T is a few μeV and the mentioned effects are smeared out or even completely covered by the always larger energy scale of thermal excitation $k_B T = 86\mu$eV /K.

2.3 Phase and energy relaxation

Electrons can maintain their phase memory until a phase randomising event, like an inelastic scattering with a large change of energy, has taken place. This can be scattering with phonons or a series of small angle scattering with other electrons which is dominant at low temperatures. In an elastic process the phase coherence of the electron is not broken which gives rise to the well known quantum interference effects like weak localisation or universal conductance fluctuations.

In our experiments we are more interested in the length scale of *energy* relaxation. But since these two length scales are related the phase coherence length determined by weak localization measurements (sec.6.4) gives a good estimate for the energy relaxation length in our samples.

Chapter 3

Structuring on a submicron scale

3.1 Electron beam lithography

For the fabrication of submicron structures a scanning electron microscope (SEM) is indispensible. With a software the deflection of the electron beam can be controlled and scanned in x and y direction over the sample. For an e-beam sensitive material a polymer film, polymethylmethacrylate (PMMA), is spun on the sample. Where the electrons hit the PMMA the polymer chains break and can be dissolved with a developer (MibK and IPA in a ratio of 1:3). To make it insensitive to further illumination pure IPA is used as a stopper. The PMMA can now be directly used as evaporation mask and be dissolved afterwards (lift-off technique) or it can serve as a template for further structuring of the material below. The electrons of the e-beam contribute only to a small part to the chain breaking. More effective are the backscattered electrons from the substrate. Since these electrons are emitted in a wide angle the resolution of the lithography is always below the best spot size of the SEM and is dependent on the substrate material.

To our disposal was a Jeol JSM-IC848 SEM with a lithography software from Raith with a motorised stage, a custom made beam blanker and an external field compensation. To improve the resolution on highly insulating materials a 5 nm thin layer of titanium was evaporated on top of the substrate to avoid charging of the surface. A relatively thick (750 nm) film of PMMA was spun on the sample which was a tradeoff between good lithography resolution and the requirement to use the resist in the next process step as a reactive ion etching mask. Due to the backscattered electrons there is a kind of flood illumination of the PMMA from the backside. When two structures are very close together (below 3-5 micron) this must be considered in the exposure dose (Fig. 3.1).

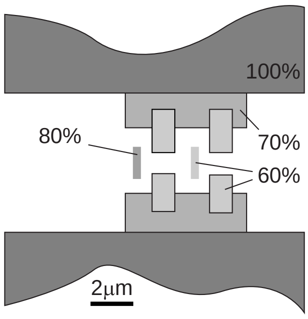

Figure 3.1: Electron beam exposure dose with proximity correction. If objects get very close to each other the required exposure dose is lower due to the backscattered electrons from the elements nearby. 100% corresponds to the correct dose for an isolated element.

pattern	dose
single thin line	$3.7\,\mathrm{nC/cm}$
area of lines	$3\,\mathrm{nC/cm}$
small area (stepsize 8 nm)	$406\,\mu\mathrm{C/cm^2}$
large area (stepsize 200 nm)	$450\ \mu\mathrm{C/cm^2}$

Table 3.1: Exposure dose for 750 nm thick PMMA and different patterns.

In some more recent programs this proximity correction is implemented in the pattern generator software but in our case it had to be done empirically. Due to software limitations it was difficult to produce small rectangles with sharp corners. Instead, the structures had more a "dogbone" shape (Fig. 3.2), presumably because the beam stayed at the end of a line scan for a short time before starting the next one. Another problem was an artefact of the beam blanker. When starting a new pattern the beam was not stabilized fast enough on its new position. The drift together with the deflection of the first line scan caused a line which merged asymptotically to the structure. The best results where obtained by a meander design starting in the center and covering the whole area in a spiral shape. If the distance between the lines is small enough the area in between is exposed by the backscattered electrons.

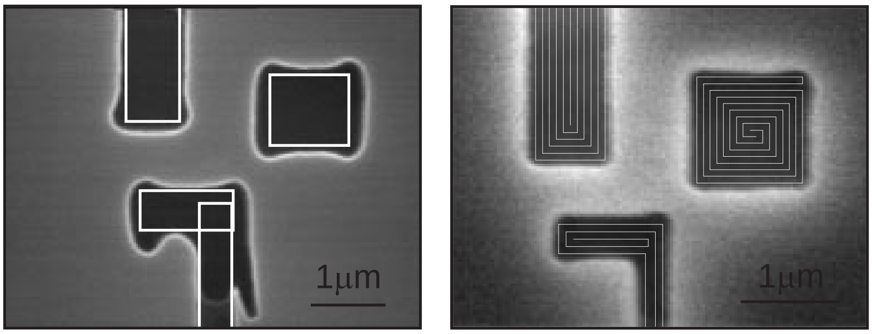

Figure 3.2: Left: structure in PMMA when areas are defined as squares in the pattern generator programm Proxy. Right: structure when lines are used to fill the squares. The lines start and end in the center of the structure.

3.2 Reactive ion etching

In microstructuring it is often necessary to transfer the soft PMMA pattern created by e-beam lithography to a nonorganic hard material. The PMMA is then used as a template to structure the material below. This can either be done by wet chemical etching or dry etching in a plasma chamber. For the selective and anisotropic etching of materials we used the reactive ion etching (RIE) machine Plasmalab^{plus} from Oxford Instruments. The mechanism of ablation is either a purely physical, by heavy ion bombardement (i.e. Argon), or a chemical, where highly reactive ions like chlor or fluor are used. The first is mainly used for surface cleaning or structuring of nonreactive materials like the noble metals. The reactive etching can result in higher etch selectivity between mask and substrate material.

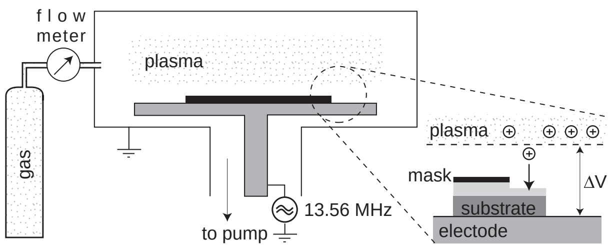

Figure 3.3: Sketch of a RIE machine. For explanation, see text.

To create a plasma a high frequency (HF) field is applied between the substrate electrode and the chamber wall. In the gas are always some ions present from radiation ionization. At low pressure the electrons can pick up enough energy between collisions to cause further ionization. This avalanche effect can be seen as a glow discharge (plasma). The plasma is formally neutral but since the electrons are light and have high energy they diffuse faster then the heavy ions in the HF-field, leaving an excess of positive charge in the plasma. The plasma is a good conductor so that the voltage drop appears across the boundary zone between the plasma and the substrate where no ionization takes place any more. Positive ions are accelerated through this zone and strike the substrate at near-normal incidence. The magnitude of the voltage drop is a function of HF-power, gas pressure and geometry of the chamber. Selectivity, anisotropy and etch rates can hardly be predicted and each process must by empirically installed. In table 3.2 some of the processes are listed with the corresponding parameters.

function name	gas	pressure [torr]	HF-power [Watt]	voltage [V]	etch rate [nm/min]
sputtering	Ar	0.02	150	500	Au 15
					PMMA 82
cleaning	O_2	0.025	100	416	PMMA> 200
		0.8	50	90	Photores. 190
Si_3N_4etch	CHF_3	0.025	100	411	Si_3N_4 35
	+				Si 9
	10% O_2				PMMA 100

Table 3.2: RIE process parameters

3.3 Sample carrier for projection imaging

For some experiments it is interesting to have the sample (i.e. a wire) freely suspended between two contact pads instead of lying on a substrate. For example, nanotubes are supposed to change their electrical transport properties when they are attached to the substrate by Van der Waals force. But the main purpose of the fabricated sample carrier was to image DNA with a low energy electron projection microscope (LEEPS) and simultaneously perform transport measurements. In order to realize this we used a 170nm thick silicon nitrid membrane which covered a $1\times$ 3 mm^2 window in a silicon wafer. To obtain a slit in the membrane with contact pads on both sides, PMMA was first used as an evaporation mask for gold (lift off-process) and in a second lithography step as a mask to etch a slit into the membrane. The first lithography defined the gold structure of two large contact pads and fine leads which where only separated by a few micrometer. The leads had to go outside the membrane in order to have a solid substrate for the wire bonding. In a second lithograpy a window in the PMMA was defined which covered a part of the gap between the gold leads. For the subsequent RIE the gold on the long side and the PMMA at the ends defined the etch mask for the slit in the membrane. To use gold as an etch mask has the advantage that the borders of the slit are conducting. This is indispensible for the electron projection microscopy where trapped charges on insulating areas can strongly distort the image. This structuring method is being futher refined by a member of our research group.

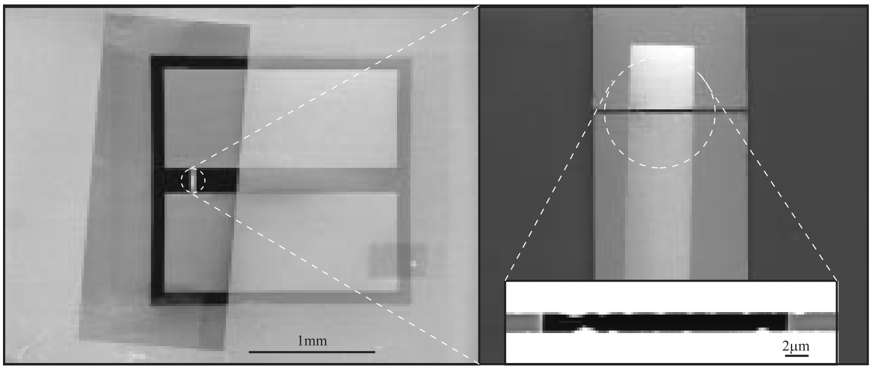

Figure 3.4: Slit in a Si_3N_4 membrane. Left: the slightly tilted rectangle is the membrane across a 1×3 mm window in a Si wafer. The bright parts are the gold contact pads which go from the solid substrate onto the membrane where they are only separated by a few micrometers. Right: zoom of the centerpart. Across the gap in the gold structure a second PMMA window is defined and by RIE the area which is surrounded by either gold or PMMA is anisotropically etched (right inset).

3.4 Nonorganic evaporation mask

Recently, several groups [26] have encountered the problem that submicron niobium structures patterned with ordinary PMMA resist had a significantly suppressed transition temperature T_c compared to the T_c of a coevaporated niobium film. The most important reason is the outgassing of the PMMA. The contamination of the material takes place during the evaporation of the high melting Nb. Due to radiation heating from the evaporation source, the PMMA gets so hot that molecular components of the resist can sublime and be integrated into the metal film. This was recently confirmed by a group from Grenoble [1]. They measured the loss of weight as a function of temperature. For PMMA they observed a significant loss already at only 150°C. This is a temperature that can easily be reached during e-beam evaporation. Most experiments which involve superconductors have therefore been performed with low melting materials (e.g. Al). However niobium based junctions are very interesting because of the larger superconducting gap (Δ) which allows to study a wider energy range of temperature and magnetic field dependent effects. An established method to fabricate junctions with well defined interfaces is the use of angle evaporation through a suspended mask [27]. By varying the angle between the substrate and the evaporation source one can fabricate very clean interfaces with small overlap or wires of very narrow linewidth. The commonly used method for shadow evaporation is e-beam lithography in a double layer resist. Two different photoresists with different sensitivity provide high resolution pattern with a suitable undercut profile [28]. The double layer resist of PMMA as mask and a co-polymer (PMMA-MA) as support has shown to be successful for low melting materials [29]. For high melting materials more complicated techniques were developed like a two layer metal mask which was differentially etched [30] or a four layer resist system [26]. The first is not applicable for angle evaporation of submicron structures because of the rough edges of the mask. The latter still had the problem of deterioration of the superconducting properties. The T_c was suppressed down to 1/5 of its bulk value. To have a thermally stable resist is most important for small devices where the whole structure is in the vicinity of the mask material.

For this reason we have developed a nonorganic evaporation mask. Figure 3.5 shows a chart of the process. We start with a 800 nm SiO_2 and a 200 nm Si_3N_4 layer on a Si wafer. Both materials were deposited by Low Pressure Chemical Vapor Deposition (LPCVD). On the Si_3N_4 a 600nm PMMA layer is spun. The PMMA top layer is structured by conventional e-beam lithography (sec.3.1). After development in 1:3 MibK:IPA the PMMA is used as an etchmask for the Si_3N_4. The pattern is transferred to the Si_3N_4 by a CHF_3 anisotropic Reactive Ion Etching (RIE) process (sec.3.3). The etch ratio of Si_3N_4 to PMMA is 1/3 at 0.03 mbar and 100W. At this step we have to accept a little widening of the structure because the width of the opening in the Si_3N_4 will correspond more to the bottom width of the PMMA undercut profile, because the overhanging PMMA is etched more rapidly in the plasma (see Fig. 3.5b). Now the SiO_2 support layer can be removed with a wet etchand. 15 min in buffered hydrofluoric acid (BHF) results in the free standing Si_3N_4 with 1 μm undercut.

This technique allows to produce deep undercut profiles in a very controlled way, since only the topmost PMMA layer must be sufficiently exposed during e-beam lithography. In contrast, the ordinary double layer

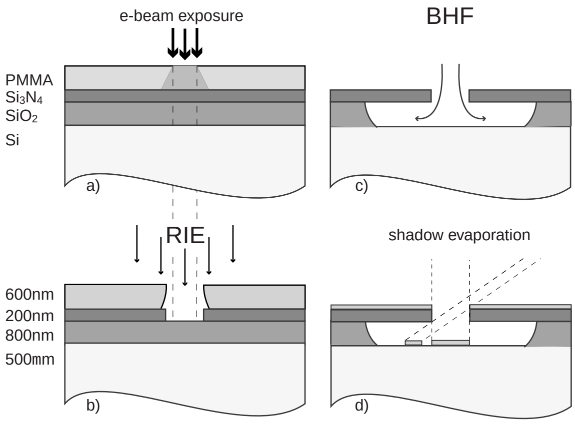

Figure 3.5: Process chart: a) e-beam lithography on a three layered wafer b) pattern transfer by RIE c) wet etching of the support material d) angle evaporation through the stencil.

technique with PMMA-MA relies on overexposure of the MA layer to achieve a large enough undercut. The Si_3N_4 stencil is mechanically strong enough that bridges of several micrometers can easily be realized. Under clean preparation conditions there is no contact between the device structure in the etched pit and the film on top of the stencil which is 800nm offset from the substrate.

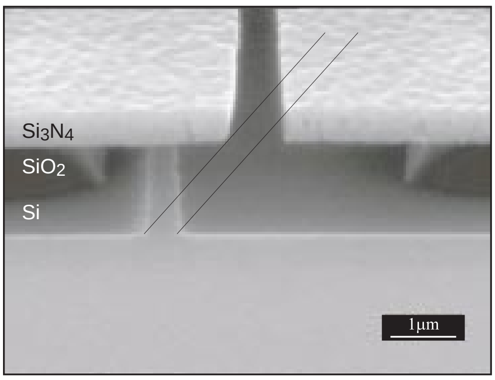

Figure 3.6: Tilted view of a Si_3N_4 layer on top of a SiO_2 spacer layer. On the silicon substrate is the metal structure which is defined by the openings in the nitride mask.

The advantage of the shadow mask are threefold. First, different materials can be evaporated subsequently without breaking the vacuum. This allows to obtain very clean contacts between the layers. In addition we can avoid oxydation and migration of the first material because the growth of the second material can follow immediately. The second advantage is self alignment. This means that overlap areas of very small size and accuracy are possible which would be very hard to achieve with an additional lithography step. Angle evaporation through the shadow mask has the advantage that fine lines get even narrower. By this, linewidths of dimensions below the resolution limit of the e-beam lithography can be realized, which is not necessarily the resolution of SEM but the linewidth after the etching. The diameter reduction factor of the slit in the mask and the wire on the substrate in the left side of figure 3.7 is 2/3. The mask can not be simply removed with a solvent like in the ordinary lift-off process. But still it is possible to make a sort of mechanical lift off at the positions where the Si_3N_4 is strongly underetched. For experiments where magnetic field effects are of interest and superconducting materials are used it is advantageous to remove the mask. Otherwise it is very difficult to know where the flux is penetrating the sample and where it is repelled. To perform a lift-off, a strongly diluted PMMA ($\sim 2\%$) was spun onto the sample. The viscosity of the PMMA must be low enough to enable wetting below the mask. Ontop of the thin PMMA layer highly concentrated PMMA was deposited. When the PMMA has dried it forms a macroscopic rigid film that can be grabbed with a tweezer. When lifting the PMMA film it takes the free standing parts of the sample with it (Fig.3.7). Instead of spinning PMMA, ultrasonic can be used to enhance the diffusion of the PMMA below the mask. Our mask is chemically absolutely stable and can even be used in ultra-high vacuum (UHV) evaporation chambers in which heat treatments are used to clean the chamber and sample. The latter is important for the deposition of fine magnetic layers.

3.5 E-beam evaporation

The metal deposition was done by e-beam evaporation in a *Balzers PLS* 500 system. The e-gun is equiped with four revolving targets which can be rapidly changed. The film thickness of the evaporated material is measured by a quarz resonator. With a PID controller from *Telemark* the evaporation rate can be adjusted. Liquid nitrogen cooling of the chamber walls enables a base pressure of 10^{-9} mbar. The sample is mounted on a holder that can be rotated, tilted and if necessary also cooled.

3.6 Connecting the micro to the macro world

To connect the submicrometer scale devices to the macroscopic world of the measurement equipment the fine structures open up into bondpads a few hundred micrometer in size. The silicon substrate is glued with Epoxy

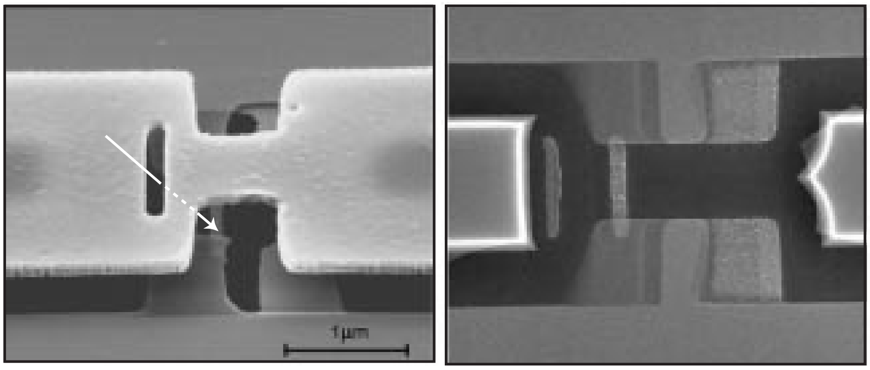

Figure 3.7: Left: silicon nitrid mask with the shadow image beneath. Two metals were evaporated under a tilt angle from the left and the right side. Right: device structure on the substrate after mechanical removal of the mask. The wire in the middle is connected to the reservoirs however the left wire which originates from the second evaporation is isolated. The bright parts are the SiO_2 spacer layer of the mask.

into a cip carrier and contacted using ultrasonic bonding of thin aluminum ($50\,\mu m$) wires (see fig.3.8). The chip carrier can now be inserted into different measurement setups. The sample inspection was done with a Philips $XL30\,FEG$ SEM.

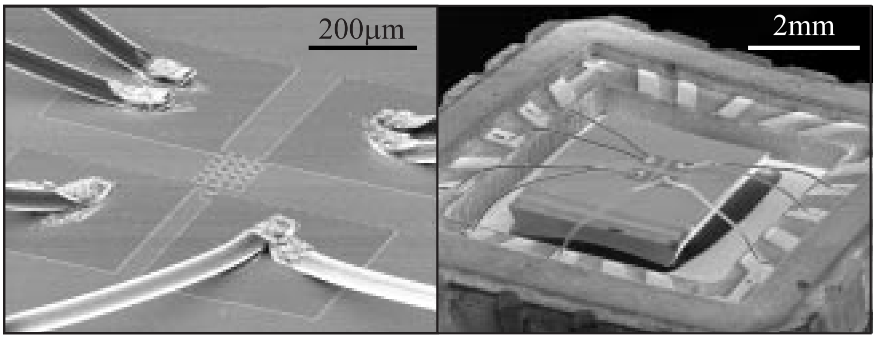

Figure 3.8: 50 μm aluminum wires attached by ultrasonic bonding to the contact pads of the device. Right: bondwires connecting chip carrier and sample.

Chapter 4

Measurement Setup

Low temperatures were needed in our experiments for two reasons. First, to cool down the superconducting materials below their transition temperatures (Nb $\approx$ 8K / Al $\approx$ 1.18 K) and second, to reduce the influence of inelastic scattering on the phase sensitive effects. The determination of T_C and its size dependence of narrow Nb wires were performed in a He^4 cryostat from Cryogenics. The transport and noise measurements were done in a He^3 cryostat also from Cryogenics which reached 270 mK.

4.1 Cooling System

In a He^3 cryostat two cooling systems are combined which both rely on adiabatic expansion. In the He^4 system the liquid helium enters through a needle valve into a small container called 1 kelvin pot. By pumping on the helium gas the temperature of the liquid helium can be lowered down to 1.4 K. The second cooling system consists of a He^3 gas container at room temperature which is connected by a long tube to a second container (He^3 pot) close to the sample holder (see fig. 4.1). The tube crosses an area with charcoal (absorbtion pump) and the 1K pot. When the absorbtion pump is hot ($\geq$ 40K) the He^3 gas condensates in the He^3 pot. The pressure in the He^3 system can be adjusted by the temperature of the absorption pump. The stronger the absorption of He^3 atoms on the surface of the cold charcoal the lower the gas pressure and in consequence the lower the temperature of the liquid He^3. The He^3 bath is connected to the sample holder by a copper bridge. The thermal coupling of the device itself is provided by the bonding wires. With all He^3 condensated in the He^3 pot the sample can be kept at 300 mK for about 10 hours.

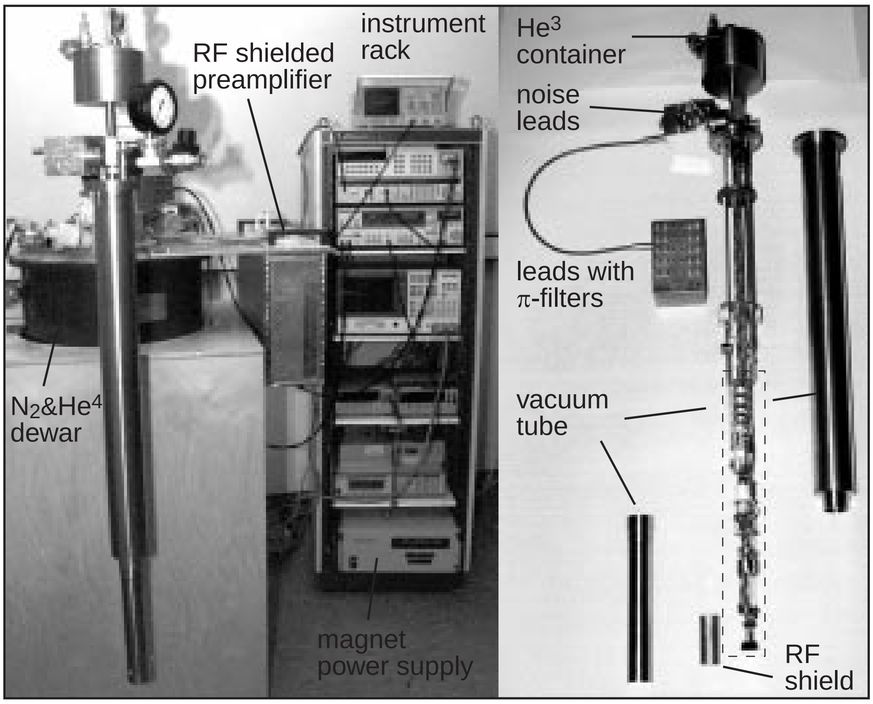

Figure 4.1: Left side: He^3 cryostat with instrument rack. The insert is hanging in front of the dewar where it is normally immersed in liquid helium. Right side: details of the insert when the tube for the isolation vacuum is removed. On top is the He^3 container at room temperature which is connected via the absorption pump and the $1K$ pot to the He^3 pot, close to the sample (see next figure). All wires have π-filters at the top of the insert, except for a set of wires used for noise measurements.

4.2 Wiring and rf-filtering

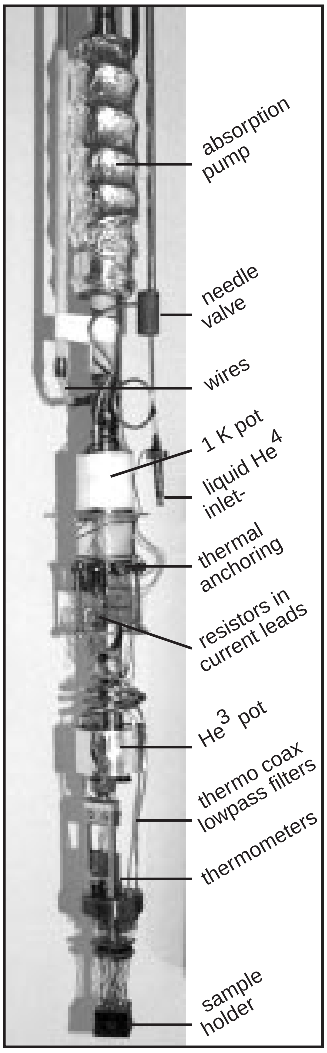

To reach low electron temperatures quite an effort has to be taken. Even when the bath temperature is low the electron temperature can be much higher due to radiation heating. The important energy scales in our experiment range from the Thouless energy of some ten millikelvin up to the Josephson coupling energy of about 10 K. The electron phonon scattering time increases with $1/T^3$. To observe mesoscopic effects an effective radiation filtering is indispensible. To attain this we equiped our sample stage with an rf-tight copper box and all wires leaving the box were Thermocoax cables from *Philips*. They consist of a wire in a fine stainless steel jacket. The insulation between wire and outer shell is made from mineral powder. The thermal conduction is nearly temperature independent and 20 times less than for copper at room temperature. The metal jacket of the Thermocoax is soldered directly to the copper box to make an rf-tight contact. The jacket around the wire has two effects: screening of microwaves and attenuation of high frequency ac currents in the wire. In the metal jacket currents are induced that counteract the HF magnetic field and hence the ac current itself. The attenuation of 40 cm coax wire is 25 dB ($dB = 20log_{10}(A_2/A_1)$ at 1 GHz (50mK) and 100 dB at 100GHz [31]. At higher frequencies, when the wavelength becomes comparable to the cross section of the coax, the attenuation is not increasing any more but is expected to be still 60 dB at 1 THz ($\sim$40K).

The resistance of the 40 cm thermo coax wire is 25 Ω and the capacitance is 230pF. This gives us a RC constant which is favorable for all ac measurements. We have made two sets of wires for our measurements. Both

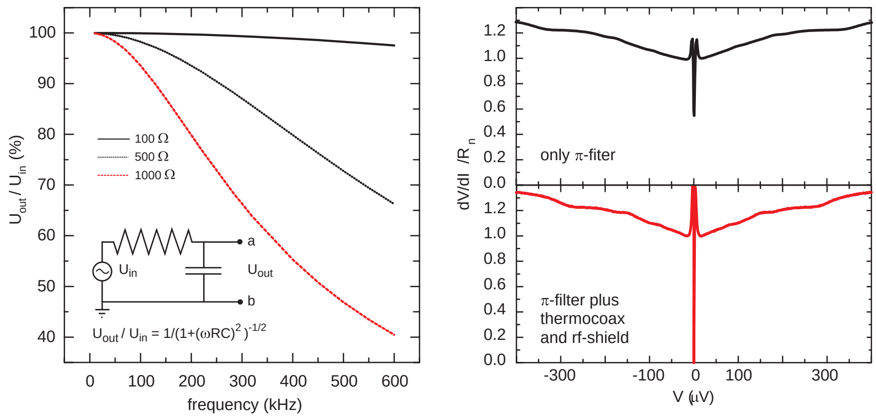

Figure 4.2: Left: amplitude suppression of voltage fluctuations in a RC-circuit for different resistances and a capacitance of 600 pF, typical for our setup. The inset is a simplified sketch of the noise measurement setup, where U_{in} represents the voltage fluctuations over the sample resistance. Right: normalised differential resistance of two 1μm long Au wires between Al reservoirs. While the sample with only π-filters at room temperature stays in an activated resistive state, the sample with copper box and the low temperature thermocoax filtering shows a supercurrent.

sets have the thermocoax at low temperatures. One set of the wires, used for noise measurements, is going directly to amplifiers kept in an rf-tight box at room temperature. At the output of the box are additional filters. These commercial π-filters have an attenuation of 70 dB up to $\sim$1 GHz and a lower cuttoff frequency at 10 MHz. The capacitance of these π filters is too high (10 nF) to have them in the noise measurement leads in front of the amplifiers. For the transport measurements a second set of wires was installed with π-filters directly at the top of the cryostat.

The effect of shielding the sample and the thermo coax filters can be demonstrated in the critical current of SNS weak links. Figure 4.2 displays the differental resistance of two series of $1\,\mu$m long gold wires of comparible resistance. When the shield is installed the sample shows a supercurrent (left curve) while a similar sample stays in an activated resistive state when the shield is absent (right curve).

Time dependent voltage fluctuations, like shot noise, are attenuated by the capacitance in the circuit which can simplified be seen as a RC-circuit like in the insert of figure 4.2. Some examples of the signal attenuation a typical total capacitance of 600 pF are shown in figure 4.2 for typical resistances and frequencies.

4.3 Noise Measurement Circuit

As shown in figure 4.3 the sample is connected through filtered leads to a floating voltage source. To have a current biased sample large series resistors in the leads are used. These resistors are at low temperatures to reduce themal noise. The voltage fluctuations accross the sample are fed into two amplifiers (*EG&G* 5184). Together with two additional preamplifiers we have a gain of 10000. Both amplifiers measure the voltage fluctuations between ground and one end of the sample. The noise spectrum is obtained by a cross correlation of the two amplifier outputs. By this, the uncorrelated amplifier noise can be strongly reduced. We obtain a resolution of $2.5{*}10^{-21}\,\mathrm{V}^2/\,\mathrm{Hz}$.

4.4 Temperature Calibration

The measured values of the voltage fluctuations can be influenced by several effects. The attenuation from the filter capacitance as described before, frequency dependent amplification of the amplifiers, background noise and perhaps some unidentified sources. The best way to take account of all these effects is a temperature calibration of the measurement setup. In a temperature ramp the measured noise is compared to the thermal noise $4k_BTR$ of a resistor. (see figure 4.3) When the data is plotted against $4k_BTR$ the slope of a linear fit to the measured noise represents the suppression factor of the whole setup. In case of figure 4.3 we have a factor of 0.92. The offset can also be corrected since the thermal noise should extrapolate to zero at zero temperature. The negative offset in fig.4.3 originates from a coupling of the amplifier noise through the common power supply. This correlated noise can not be reduced with cross correlation technique.

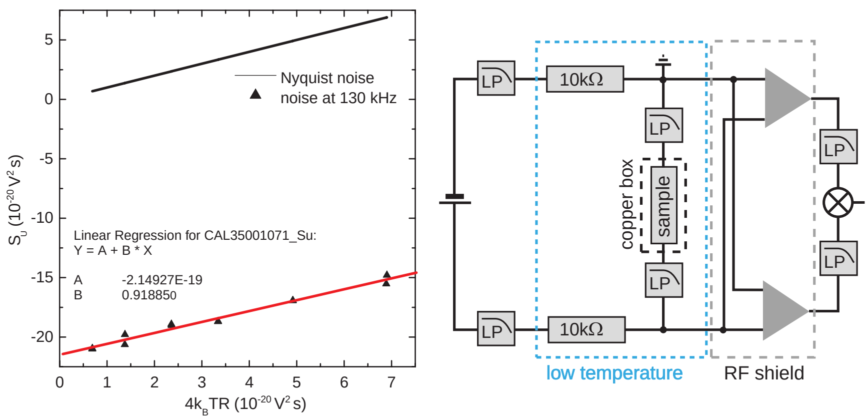

Figure 4.3: Left: Thermal noise of the sample resistance. A temperature calibration of the noise measurement setup is done by comparing the data to the theoretical Nyquist noise. Right: schematic of the setup for noise measurements. The sample is in a copper box with thermo coax filters at all leads. The large resistors at low temperature provide a low noise current biasing of the sample. The signal is fed into two parallel amplifiers and then the cross-correlation is obtained using a spectrum analyser.

Chapter 5

Reliability test of the shadow mask

5.1 Non-contaminated superconductors

As a first test of the method we produced narrow (250-415 nm) Nb wires to show that clean mesoscopic structures with good superconducting properties are feasible. The Nb wires of varying linewidth were prepared by depositing 50 nm of Nb with an electron beam gun at normal incidence and 5 Å/s at 10^{-7} mbar background pressure. The material parameters for the wires are listed in Table 5.1.

width [nm]	R(10°K) [Ω]	ρ(10°K) [$\mu\Omega$cm]	mfp [nm]	T_c [K]
250	67	15	2.5	8.41
390	111	19	2.0	8.4
415	116	21	1.8	8.39

Table 5.1: Sample characteristics

Figure 5.1 shows a SEM micrograph of the Si_3N_4 mask. The undercut (white) is about 2μm. The resistive transitions of Nb wires together with a coevaporated two dimensional (2D) Nb film are shown in figure 5.1. The transitions of the wires are very sharp and very close to that of the 2D film. The inset in the bottom figure 5.1 compares the dependence of T_c on wire width for both the Si_3N_4 and the PMMA-MA resist techniques.

While in the case of PMMA-MA T_c goes down to 2 K, for the Si_3N_4

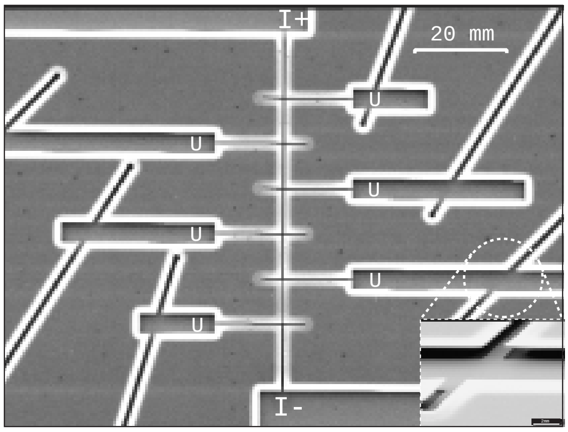

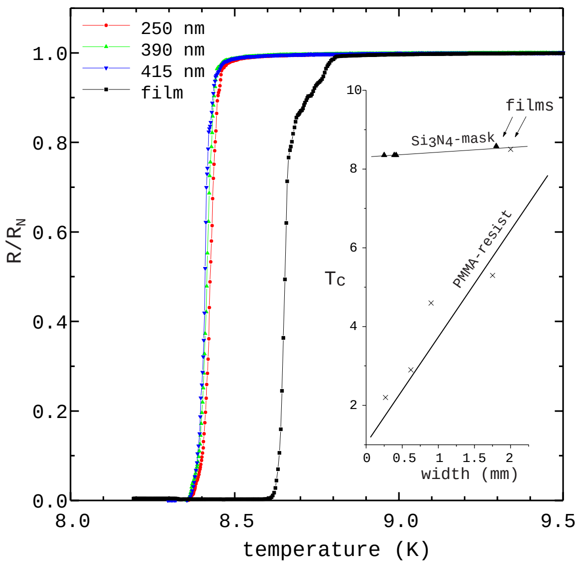

Figure 5.1: Top: Series of Nb wires with current leads on top and bottom and voltage probes to the sides. The wires are 50 nm thick and from top to bottom 1 μm to 250 nm wide. The white areas are the free standing parts of the mask. Bottom right: a detail of the mask seen under a tilt angle.
Bottom: Normalized resistance as a function of temperature of Nb wires of varying width together with a coevaporated film. The inset shows a strong decrease in T$_c$ of Nb wires fabricated with PMMA resist.

hardly any degradation can be seen! Our investigation shows that not only the background pressure during evaporation but in particular the outgassing of the organic resist mask is the main source of impurities in the deposited material.

5.2 Highly transparent interfaces

For electron transport investigations in superconductor/normal metal/super conductor (SNS) junctions we have prepared gold wires between superconducting Nb reservoirs. This was performed by evaporation under large angles where we have exploited the very large undercut and large separation between the substrate and the stencil. This allows a horizontal shift of the shadow image of several micrometers which is significantly larger than the line width. Figure 3.7 shows the pattern in the Si_3N_4 mask and the device structure that results after evaporation under two different angles. Under 33° tilt angle 15 nm gold was deposited at 5 Å/s and 10^{-6} mbar. Without breaking the vacuum 50 nm Nb was evaporated at 5 Å/s and 10^{-7} mbar under -33° tilt angle. This has the advantage that we have very clean interfaces without oxidation or adsorbates at the interfaces. Samples of gold wires between Nb reservoirs showed a strongly decreasing resistance in R(T) due to the proximity effect (Fig. 5.2). The coupling of the normal wire to the superconducting reservoirs is so strong that for a $0.4\,\mu$m long wire a supercurrent flows already at 3.5 K. This indicates the high purity of the SN junctions since the proximity effect is suppressed exponentially with the thickness of the interface barrier.

The possibility of preparing high purity materials in submicron dimensions with the option of the angle evaporation technique makes the anorganic SiN mask perfectly suitable for the fabrication of mesoscopic hybride structures.

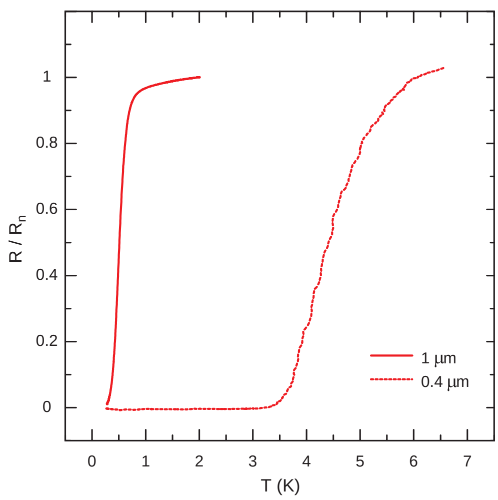

Figure 5.2: Normalized resistance as a function of temperature of 1 and 0.4 μm long Au wires between Nb reservoirs. Both show the transition to a zero resistance state and for the 0.4 μm long Au wire a supercurrent of 41 μA at 0.3 K.

Chapter 6

Super/Normal/Super conductor junctions

Nanofabrication allows to structure hybrid mesoscopic NS devices in which a lot of phenomena have been discovered which are attributed to Andreev reflection (AR) and the proximity effect. The phase sensitivity of AR and the picture that Andreev-reflected holes travel the time reversed path was demonstrated by Van Wees *et al.* in an Andreev interferrometer [32]. The two ends of an open superconducting ring were connected to a two dimensional electron gas (2DEG). The current that leaves the 2DEG at a well defined point contact was measured. It was shown that electron and hole travel the same path and carry the information about the phase of the superconductor. The phase difference at the ends of the open superconducting ring led to constructive or destructive interference in the point contact and could be probed as conductance oscillations.

So-called "*Reflectionless*" tunneling was observed at NS interfaces in contact with a diffusive normal wire. Here, inelastic scattering in N redirects the electrons to the interface and increases the probability of transmission [33]. Non-local effects at distances of order L_{Th} have been demonstrated in samples where the superconductor was in contact with the normal part, but not directly in the classical current path [21]. It was discovered that the phase sensitive contribution to the magneto conductance is described by a $1/T$ power law and is much larger than the weak localisation correction. The *reentrance* to the normal state conductance of a NS interface has been understood in terms of an energy dependent modification of the density of states in the normal part [20, 19]. The transport through Andreev bound states [23] and its manipulation by varying the occupation probability has been used for a *hot electron* transistor [24].

Our work has been focused on the consequences of Andreev reflection to the shot noise in SNS devices. Important components are the absence of energy transfer through the NS interface and multiple particle transfer. In this chapter we will present measurements on SNS junctions which reveal these unique properties for electric charge and energy transfer. In a SNS junction an electron is Andreev reflected at one side of the junction as a hole. This hole is again Andreev reflected at the other interface as an electron and so forth. In each cycle a Cooper pair is transmitted and the energy $2eV$ is gained. When the energy is larger than the gap energy Δ, the back and forward propagating quasiparticles can enter the superconductor and the cycle is terminated. The kinetic energy of the quasiparticle is now transferred to the superconducting reservoirs. By passing a current through the SNS junction a strong out of equilibrium electron distribution is created in the normal metal which can be monitored by electronic noise measurements. In a second experiment we were studying the conductance and the noise for signatures of multiple charge transfer in subsequent Andreev reflections (MAR).

In the case of normal reservoirs the distribution function $f(\epsilon)$ in the wire either assumes a two step shape if the inelastic scattering length $L_{in}(\epsilon) \gg L$, or smears out into a Fermi-Dirac function with a spatially varying electron temperature if $L_{in}(\epsilon) \ll L$ (sec.2.1) [34, 35, 36]. The broadening of $f(\epsilon)$ has been detected by local tunneling spectroscopy [35], or by measuring the power spectral density $S_V(V)$ of the current noise in the junction [36, 37, 38].

In the case of superconducting reservoirs the broadening of $f(\epsilon)$ is expected to be much more dramatic when compared to normal reservoirs. In particular for small applied voltages $eV \ll \Delta$ quasiparticles have to climb up to the energy gap Δ via multiple Andreev reflections (MAR) at the two SN boundaries in order to remove energy from the normal part into the reservoirs.

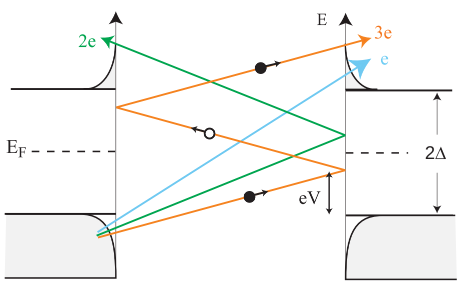

Figure 6.1: Schematic of a multiple Andreev reflection process between two NS interfaces. The quasiparticles can only enter the superconductor when they have gained energy larger than the gap. This energy can be acquired by several transversals of the applied voltage.

For no inelastic scattering in N a sharp rise in the differential conductance dI/dV is expected at voltages of $2\Delta/en$ where n counts the number of reflections in the MAR cycle (subharmonic gap structure). Such structures have been found earlier in superconducting microbridges, tunnel junctions and ballistic S/N/S point contacts [39]. Subharmonic gap structures have also been observed in diffusive samples [40]. In addition there are experimental indications that the coherent MAR cycle transfers multiple charge quanta of magnitude $2\Delta/V$, which should lead to an enhanced current noise at low bias voltages [41]. For diffusive systems charge doubling has been reported recently for an NS interface which points towards single Andreev reflection events [42].

In our experiments we address the above questions by measuring dI/dV and S_V of high transparency Nb/Au/Nb, Al/Au/Al and Al/Cu/Al junctions. Compared to previous studies[43] we focus on junctions having a very small critical current.

6.1 The samples

Our SNS devices consist of thin ($\simeq$ 15 nm) normal wires (Au or Cu) of 0.4 - 2 μm length and 100 - 200 nm width between thick (50 - 200 nm) reservoirs made of Nb or Al. A scanning electron micrograph of a Nb/Au/Nb sample is shown in Fig. 6.2. The materials are evaporated under 33° tilt angle from the left (N = Au) and the right (S = Nb) side respectively.

A single SNS junction and a series of 9 - 16 junctions together with 20 μm long N and S wires were prepared simultaneously on the same chip. The measurements were performed in a ^{3}He cryostat which is shielded from rf interference by π filters at room temperature and by a thermocoax filtering stage at the 0.3 K stage.

Table 6.1 lists the parameters of two typical samples presented in the following sections.

sample	L $[nm]$	w $[nm]$	t $[nm]$	$R_\square$ $[\Omega]$	ρ $[\mu\Omega cm]$	D $[m^2s^{-1}]$
Nb/Au/Nb	2000	230	15	4.8	7.2	5.18e-3
Al/Cu/Al	900	160	18	3.4	6.28	7.2e-3

Table 6.1: Material parameters of the SNS samples

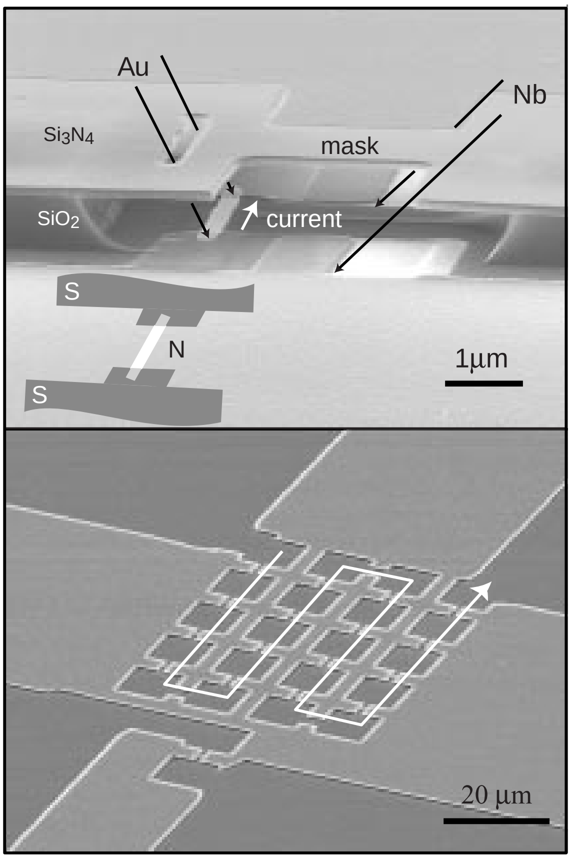

Figure 6.2: Top:scanning electron micrograph of a typical sample viewed under a large tilt angle. The normal wire between the two Nb reservoirs (top and bottom) is defined through the slit in the freely suspended nitride mask. Inset: schematic of the sample layout. Bottom: overview of 16 SNS junctions in series and a single SNS junction. The dark parts are the device structure and the bright parts the SiN mask. The arrow indicates the current path through the series.

6.1.1 Coherence length determination

To classify the physical regime of the normal metal wires we determined the phase coherence length (L_Φ) for gold and copper by weak localization measurements. The sample shown in figure 6.3 allows us to characterize two materials at a time. For example both materials which are used for SNS divices. By changing the tilt angle we have two parallel wires fabricated under identical conditions which can be measured in a four terminal configuration. At temperatures below 1K the dominant phase-breaking mechanism in nonmagnetic disordered metals is electron-electron scattering. The corresponding phase-breaking rate decreases as the temperature is lowered with a power law, $\tau_\phi^{-1} \propto T^p$ where p depends on the dimensionality of the system. In a normal metal the simplest means to obtain L_Φ is to

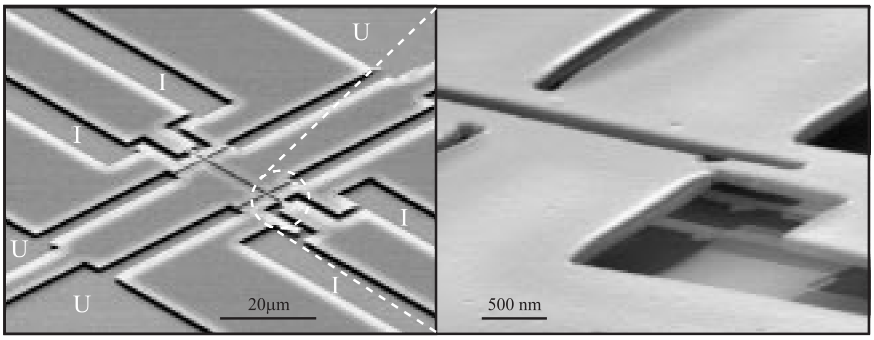

Figure 6.3: SiN mask for two parallel wires in a four terminal configuration. Right: below the mask the wires can be seen which result from evaporation under different tilt angles. The wire of material A is connected to probes of material B and vice versa.

fit the low field magnetoresistance to the theory of weak localization [44]. The effect of weak localization is a quantum correction to the conductivity. According to Ohm's law the resistance of an array of scatterers increases linearly with the lenght of the array. This holds only if the phase coherence length is shorter than the scattering length. But at low temperatures, L_Φ can exceed the mean free path. In this case the conductor must be viewed as a series of phase coherent units, with interference of different electron paths. The origin of the correction to the conductance is a largely enhanced probability of the electron to come back to the origin after a diffusive path, also known as coherent backscattering [45]. The electron can also be regarded as two partial waves travelling the same path in opposite directions. The two partial waves acquire the same phase shift and interfere constructively at the origin. The enhanced return probability of the electron (hence the name weak localization), results in a reduced conductivity. This effect is very sensitive to a magnetic field since the partial waves experience a phase shift by the vector potential and constructive interference is lost. For heavy metals like Au and Cu with strong spin orbit coupling an anti-localization is observed. The spin of the electron can be rotated on its diffusive path. Spin 1/2 particles have to be rotated by 4π to interfere constructively and it can be shown that the destructive part exceeds the constructive one [46]. This means that the back-scattering probability is reduced below the statistical one which results in an enhanced conductance.

In case of a long wire ($L >> L_\Phi$) but L_Φ >width and thickness, the weak localization correction is [47]:

$$\frac{\Delta R}{R} = \frac{R_\square}{\pi\hbar/e^2}\frac{L_\Phi}{w} \tag{6.1}$$

where $R_\square$ is the sheet resistance and w the wire width. The effect of a magnetic field can be described by introducing a field dependent L_Φ [44]:

$$\frac{1}{L_\Phi^2(B)} = \frac{1}{L_\Phi^2} + \frac{1}{3}\left[\frac{\pi w B}{h/2e}\right]^2 \tag{6.2}$$

For strong spin-orbit coupling the weak localization correction breaks up into a singlet and a triplet part [45]:

$$\frac{\Delta R}{R} = \frac{1}{2}\left(\frac{R_\square}{\pi\hbar/e^2}\frac{L_\Phi}{w}\right) - \frac{2}{3}\left(\frac{R_\square}{\pi\hbar/e^2}\frac{L_2}{w}\right) \tag{6.3}$$

where L_2 is a function of L_Φ and the spin-orbit scattering lenght L_{SO}:

$$L_2^{-2} = L_\Phi^{-2} + \frac{4}{3}L_{SO} \tag{6.4}$$

The fit to the conductance data was done by the expression below 6.5 which follows from 6.2-6.4. Terms of magnetic impurity scattering are not considered. Fitting parameters are L_Φ and L_{SO}.

$$\frac{\Delta G}{e^2/h} = \frac{1}{L}\frac{1}{\sqrt{L_\Phi^{-2} + \frac{1}{3}\left(\frac{\pi w B}{\Phi_\circ}\right)^2}} - \frac{3}{L}\frac{1}{\sqrt{L_\Phi^{-2} + \frac{4}{3}L_{SO}^{-2} + \frac{1}{3}\left(\frac{\pi w B}{\Phi_\circ}\right)^2}} \tag{6.5}$$

We measured 15 nm thick Au and Cu wires of 20 μm length, 270 nm and 300 nm width. The samples were measured in a He^4 cryostat. Resistance measurements were performed with a AC four terminal lock-in technique. The measurement sensitivity was enhanced by an Adler-Jackson bridge circuit to detect only resistance changes compared to a reference resistance. Figure 6.4 shows the magneto conductance in units of e^2/h from 1.3 to 9 K. For clarity the data is shifted vertically. Since currently there is a

sample material	L $[\mu m]$	w $[nm]$	t $[nm]$	R (3K) $[\Omega]$	ρ $[\mu\Omega cm]$	D $[m^2 s^{-1}]$	L_{SO} $[nm]$
Cu	20	300	15	285	5.85	4.17e-3	123
Au	20	270	15	281	7.2	5e-3	40

Table 6.2: Material parameters of Cu and Au wires for weak localisation measurements

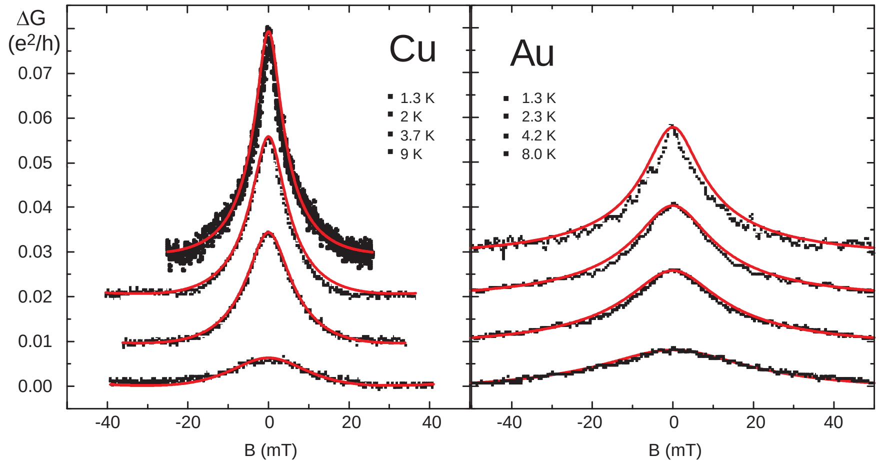

Figure 6.4: Magneto conductance of 1D Cu and Au wires at different temperatures. The fits are done to the formula 6.5 with L_Φ and L_{SO} as free parameters.

lot of discussion about phase relaxation at low temperatures we show the temperature dependence of L_Φ and τ_Φ respectively in figure 6.5. Our data is limited to temperatures larger than the T_C of the Al probes. This is not sufficient to calculate a reliable value for the power of the temperature dependence. Our data is presumably in the cross over from electron-phonon to electron-electron scattering. We do not see any saturation at low temperatures as claimed by some groups. The linear fit over the whole temperature range gives a power dependence of τ_Φ on T of -1.36 for Cu and -1.03 for Au.

6.2 Nb/Au/Nb - junctions

In Fig. 6.6 we show the differential conductance dI/dV vs. applied voltage of a single Au wire of length $L = 1\,\mu$m between Nb reservoirs. The inset displays $R(T)$ for the same sample. The data are recorded using ac currents of typically 10 and 20 nA. When lowering the temperature the resistance first drops around 8.2 K which indicates the superconducting transition of the reservoirs. Further reduction of the temperature leads to a continuous decrease of R which becomes more drastic below 2 K. This proximity induced reduction of R is accompanied by a sharp peak in the differential conductance dI/dV at zero bias voltage. The peak has a width of 50 μV (which is close to k_BT at 0.3 K) and can be seen as the precursor of a super-

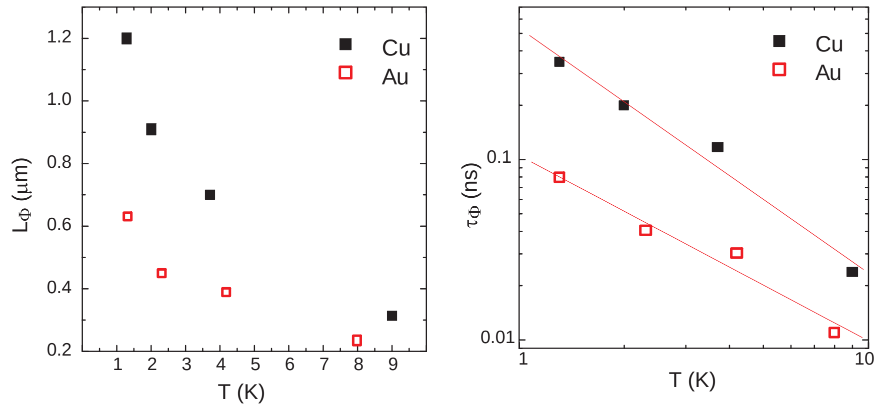

Figure 6.5: Phase coherence length L_Φ and the corresponding scattering time $\tau_\Phi = D/L_\Phi^{-1/2}$ for copper and gold. The slope of the fit to the scattering time is -1.36 for Cu and -1.03 for Au.

current which emerges when L_T becomes comparable to the wire length L. The peak has a height of only 10 % of the normal state resistance R_N of the wire for $L = 2$ μm, while we find supercurrents up to 50 μA for $L = 0.4$ μm in samples with Nb banks.

In Fig. 6.7 we present the excess noise S_V of a series of 9 Nb/Au/Nb junctions with 2 μm long Au wires. The spectral density S_V of the voltage fluctuations across the sample is measured as a function of current bias in the frequency range between 100 and 400 kHz with a cross-correlation technique [38](sec.4.3). As a reference measurement, we first collected data in a perpendicular magnetic field of 6 T in which the Nb reservoirs are normal (open squares). For a direct comparison of the (effective) electron temperatures T_{el} we have normalized S_V with dV/dI (see right-hand scale). For lower voltages $V < 1$ mV the measured noise falls on the 1/3 reduced shot noise (dashed line). At higher voltages, additional cooling via electron-phonon scattering results in a negative curvature of S_V [48].

In the case of superconducting reservoirs (solid circles) we find a dramatic increase of S_V in particular for the smallest voltages. The normalized excess noise rises with nearly vertical slope at $V = 0$ and merges at $V \sim 2\Delta/e$ into the 6 T curve. For energies smaller than the gap energy, Andreev reflection is the dominant transport channel. Via this process no energy can be transferred through the NS interface (sec.2.2.1). For higher electron temperatures the distribution function in the normal metal broadens until there is an energy overlap of excited states in N and in S (sec.6.8). Note that T_{el} is already $\simeq 6$ K for $V \simeq 2\Delta/e$. From weak localization mea-

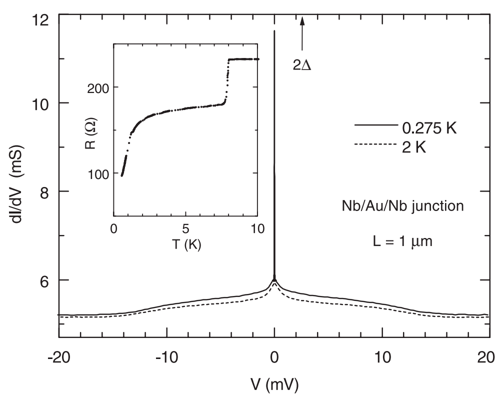

Figure 6.6: Differential conductance dI/dV of a single Nb/Au/Nb junction as a function of voltage V for two temperatures. The sharp peak at $V = 0$ indicates the rapid destruction of electron-hole coherence by a finite bias voltage. The arrow indicates $V = 2\Delta/\mathrm{e} = 2.6$ mV. Note the absence of subharmonic gap structures. The Au wire is 1 μm long, 130 nm wide and 15 nm thick. The thickness of the Nb reservoirs is 50 nm. Inset: Resistance vs. temperature for the same sample.

surements on the long Au wire we infer $L_\phi = 0.63$ μm at 1.3 K (0.39 μm at 4.2 K). Since L_ϕ is considerably shorter than the wire length of 2 μm the MAR cycle is incoherent. This is confirmed by the absence of subharmonic gap features in dI/dV (see Fig. 6.6).

The electron temperature in the Au wire is controlled by the power dissipation in the wire, the energy loss via quasiparticle transmission through the S/N interfaces, and the electron phonon scattering in the Au wire [38]. At low T_{el} the electronic heat diffusion within the Au wire is much faster than the energy loss across the interfaces so that we may assume local thermal equilibrium with a nearly constant temperature profile along the wire. The heat transfer through the interfaces can be reasonably well described in terms of a simple BTK-like expression [16] for the heat current $P_{NS}(T_{el})$ through the N/S boundaries:

$$P_{NS}(T_{el}) = \frac{2}{R_m e^2} \int_{-\infty}^{\infty} \epsilon \, (f_N - f_S)\, (1 - A - B)\, d\epsilon \ . \qquad (6.6)$$

Here, R_m is the normal state resistance of the N/S boundary, $f_N(T_{el})$ and $f_S(T_{Bath})$ are the Fermi functions in the wire and the reservoirs, while $A(\epsilon, Z)$ and $B(\epsilon, Z)$ are the coefficients of Andreev- and normal reflection and Z is the interface parameter (sec.2.2.1). We estimate $R_m \simeq 5$ Ω. Within

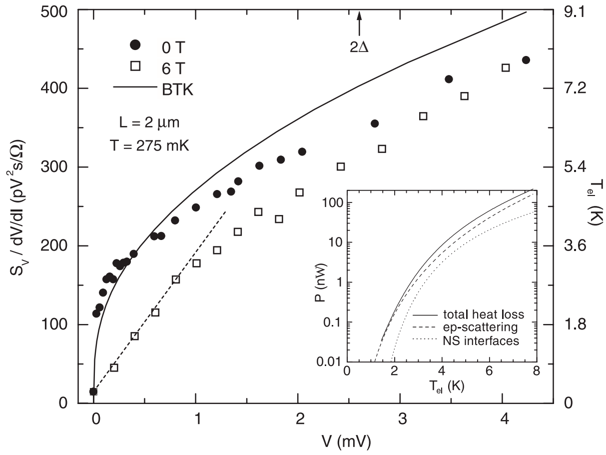

Figure 6.7: Scaled excess noise $S_V/dV/dI$ as a function of voltage for a series of 9 Nb/Au/Nb junctions of 2 μm length, 200 nm width and 15 nm thickness for normal (□) and superconducting (•) Nb reservoirs. The arrow indicates $V = 2\Delta/\mathrm{e} = 2.6$ mV. The zero bias resistance per junction is 39 (72) Ω at $B = 0$ (6) T and the diffusion constant of the wire is $D \simeq 68$ cm^2/s. At 6 T the Nb reservoirs contribute significantly to the junction resistance. The right-hand scale indicates the effective electron temperature. The dashed line indicates the shot noise of noninteracting electrons in case of normal reservoirs. The solid line gives an estimate of the electron heating effect according to Eqs. (1) and (2). Inset: Electron-phonon (dashed line) and N/S interface (dotted line) contributions to the cooling power as a function of electron temperature T_{el} in the wire. T_{el} in the reservoirs is assumed to remain at 0.27 K.

our simplified model, the cooling via electron phonon contribution scattering is given by

$$P_{ep}(T_{el}) = \left(\frac{k_B}{e}\right)^2 \frac{L^2\Gamma}{R_N} \left(T_{el}^5 - T_{Bath}^5\right) , \qquad (6.7)$$

where L is the length of the normal wire and $\Gamma \simeq 5 \cdot 10^8$ K^{-3}m^{-2} for Au [38]. The parameter Γ is related to the electron-phonon scattering time: $\tau_{ep}^{-1} = \zeta(3)/2\zeta(5)\, D\Gamma\, T_{el}^3$, where $\zeta(n)$ is the Riemann Zeta-function [49]. The calculated cooling power according to Eqs. (1) and (2) is plotted as a function of T_{el} in the wire (dotted and dashed line) in the inset of Fig. 6.7. For simplicity we assume $Z = 0$. The solid line is the sum of both contributions and corresponds to the solid line in the main figure 6.7. The plotted noise behaviour is the thermal noise $4k_BTR$ for a temperature that equals

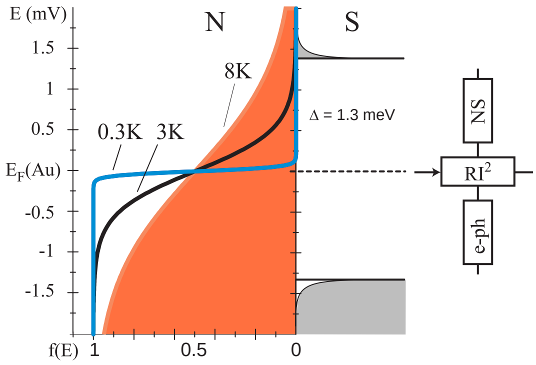

Figure 6.8: Fermi distribution in a gold wire for different temperatures. Quasiparicle and energy transfer is only possible if $f(E)$ is broader than the gap of the superconductor. The current induced energy in N can be carried away either by quasiparticles across NS or by e-ph scattering.

$P_{NS}(T) + P_{ep}(T) = U^2/R$. Finite values of Z lead to a shift of the solid lines to lower cooling power and to higher electron temperatures, respectively. At intermediate temperatures both contributions are of comparable magnitude, while the electron-phonon term wins at low temperature because of the exponential cut-off of the N/S interface term and at high temperature because of the strong T_{el}^5 - increase of the electron phonon term. In our geometry where the area of the N/S interface is tiny (200×200 nm^2), the N/S interface term is much smaller than in the related experiment on Nb/Al/Nb junctions by Jehl *et al.* [42], who used subtractive structuring of a Nb/Al-bilayer. This may be the reason, why heating effects appear to be negligible in the latter experiment.

By means of noise measurements we have shown that multiple Andreev reflections in a normal metal wire sandwiched between two superconductors lead to substantial electron heating in the wire. The strength of this heating effect depends on the size of the gap in the superconductors. For Nb with a large gap the effective electron temperature raises already for small currents up to several K, which leads to a suppression of coherent multiple Andreev reflection.

6.3 Al/Cu/Al - junctions

It is now very interesting to look at samples, in which $L_\phi(\epsilon)$ remains larger than the wire length. To avoid inelastic scattering with phonons, it is necessary to keep T_{el} below $\simeq 1$ K in the voltage range $V \leq 2\Delta$. In a second set of experiments we replaced Nb by Al, having a much smaller gap Δ_{Al}. As a consequence, the energies acquired in the MAR cycle are much lower and we expect to enter the regime of coherent Andreev reflection. For the normal wire we used both Au and Cu, where for Cu we measured a longer phase coherence length of 1.2 μm at 1.3 K than for Au.

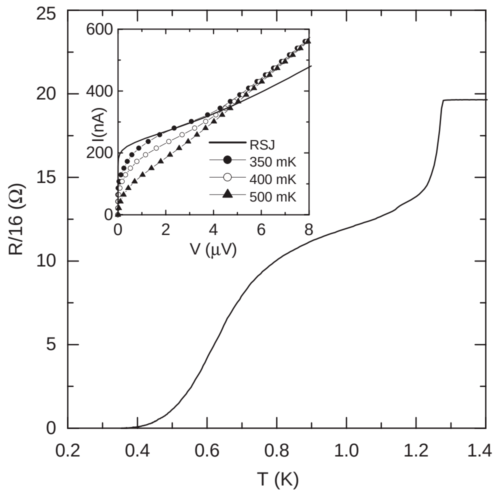

Figure 6.9: Resistance vs. temperature of a series of 16 Al/Cu/Al junctions. The Cu wires are 0.9 μm long, 160 nm wide and 18 nm thick and have a diffusion constant $D \simeq 72$ cm^2/s. The thickness of the Al reservoirs is 150 nm. Inset: Current-voltage characteristics in the low voltage region. The symbols are the experimental data and the thick solid line is a fit according to the RSJ model using $I_c \simeq$ 270nA.[18]

Figure 6.9 shows the resistance vs. temperature of a series of 16 $\times$ 1 μm long Al/Cu/Al junctions. When lowering T the resistance sharply drops at the transition of the reservoirs $\simeq 1.25$ K and then continuously vanishes as the proximity effect drives the Cu wire into a superconducting state. This sample shows zero resistance at the lowest T since the Thouless energy $E_c = \hbar D/L^2 \simeq 5\mu$eV and the normal state conductance are larger compared to the Nb/Au/Nb junctions. According to the theory by Wilhelm *et al.*[43] the critical current $I_c(T)$ reads in the limit $k_B T \gg E_c$:

$$I_c(T) = \frac{3.0\,\mathrm{mV/K}}{R_N\sqrt{T_0}}\, T^{3/2} \exp\left(-\sqrt{T/T_0}\right) \ , \tag{6.8}$$

where $T_0 = E_c/2\pi k_B$.

The inset of Fig. 6.9 displays the measured current-voltage (IV) characteristics of the same sample. The turning point of the IV curves indicates $I_c(350\,\mathrm{mK}) \approx 300\,\mathrm{nA}$. With our sample parameters we estimate from Eq. 6.8 a critical current $I_c(350\,\mathrm{mK}) \simeq 510\,\mathrm{nA}$. This estimate is reasonably close to the measured values. On the other hand, we observe a substantial broadening of the transition such that the zero voltage state is reached only for currents $\lesssim 80$ nA.

At finite temperatures a certain intrinsic broadening of the IV curves is expected by virtue of thermally activated phase slips which is usually described within the RSJ model (sec.2.2.4) [18]. Our SNS junctions are self shunted with R_N as the shunt resistance and a negligible capacitance. We observe a broadening which is much stronger than expected from the RSJ model. This is illustrated by an RSJ fit [50] using $I_c = 270\,\mathrm{nA}$ and $T = 350\,\mathrm{mK}$ which is represented by the thick solid line in the inset of Fig. 6.9. In principle such an enhanced broadening can be caused by external electromagnetic interference inducing currents larger than I_c. At high frequencies this source of broadening is suppressed by our rf filtering at room temperature and the sample stage. At low frequencies we have checked, that the highest spikes in the frequency spectrum correspond to current noise below 1 nA/$\sqrt{\mathrm{Hz}}$, which is much lower than the critical current at 350 mK. We are therefore confident that there is an intrinsic origin of the broadening of the IV curves. At voltages $V \gtrsim 5\,\mu\mathrm{V}$ the measured currents become larger than the fit. This is caused by the excess current induced by the Andreev reflection (see the discussion below).

Being made for tunnel junctions, a failure of the RSJ for long SNS junctions is not too surprising since it takes into account only the phase degree of freedom of the pair amplitude $F(x) = \langle \psi_\downarrow \psi_\uparrow \rangle$, while it neglects spatial variations of the absolute value $|F(x)|$. In SNS junctions there is a minimum of $|F(x)|$ at the center of the N-wire (fig.6.10).

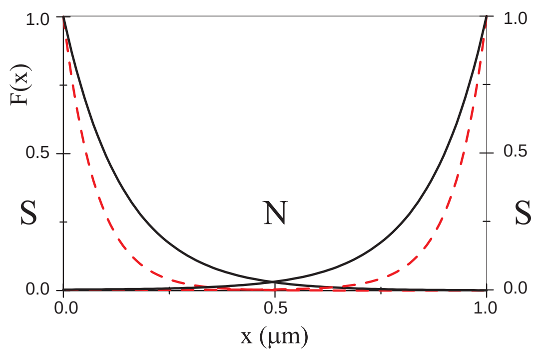

Figure 6.10: Dependence of the pair amplitude in Cu on the distance from the NS interface ($F(x) \propto exp(x/L_T)$. For 0.3 K (solid line) there is a weak ouverlap of the two pair amplitudes, which enables a supercurrent, whereas for 1 K (dashed line) this has already disappeared.

The minimum value of $|F(x)|$ at this 'weak spot' strongly depends on the ratio L/L_T which is reflected in the temperature dependence of I_c at temperatures $k_BT \ll \Delta$ described by Eq. 6.8. We believe that the enhanced rounding of the IV curves is related to the presence of the weak spot in the N-wire, which greatly facilitates phase slips in long SNS junctions. In the tilted wash board model (2.2.4) a fluctuation of $|F(x)|$ would correspond to a fluctuation of the amplitude of the potential wells *and* the slope of the wash board. Correspondingly, also the shape of R(T) cannot be fitted with the RSJ formulas, since the temperature dependence of I_c is superimposed on that of the thermal activation process. In particular, $R(T)$ does not follow a simple Arrhenius law which should be applicable for a thermally activated process with constant barrier hight. Broadened transitions induced by phase slip processes also occur in microbridges and long filaments made from homogeneous superconductors. The latter examples differ from SNS junctions in that the main temperature dependence comes from $\Delta(T)$, which is not important at our lowest temperatures.

The dI/dV curves of the same sample but in a larger voltage range are presented for various temperatures in Fig. 6.11. Besides the supercurrent

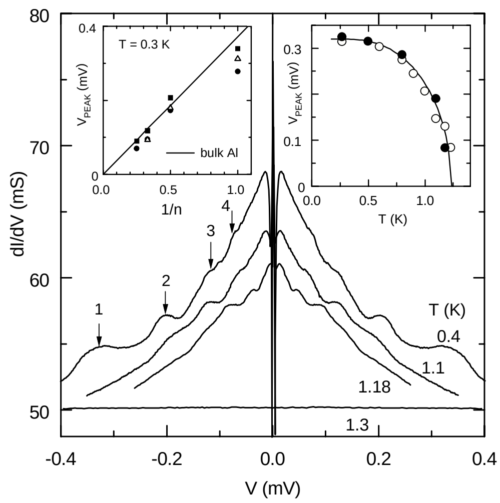

Figure 6.11: Differential conductance dI/dV vs. voltage V of the same sample as in Fig. 6.9 for several temperatures. The arrows indicate subharmonic gap structures corresponding approximately to integer fractions of 2Δ. Left inset: Position of the conductance peaks vs. $1/n$ for different samples. Right inset: Position of the 2Δ conductance peak vs. temperature for two samples with different normal state conductance ($\bullet$: 50 mS, $\circ$: 29.3 mS). The solid line is a BCS fit for 2Δ =325 μeV and T_c = 1.23 K.

at $V = 0$ we find a considerable conductance enhancement for $V < 2\Delta$. In addition, conductance peaks close to $V = 2\Delta_{Al}/ne$ are present, which we attribute to coherent MAR cycles. The peaks are rather broad and the $n = 3$ peak appears even to be split. The left inset shows the scaling of the peak positions with $1/n$. The right inset in Fig. 6.11 displays the temperature dependence of the $2\Delta/e$ (i.e. $n = 1$) peak. The peak voltages nicely match the BCS curve with a slightly reduced gap. Being governed by $L_\phi(T) \propto T^{-1/3}$ [40], the amplitude of the MAR features shows a relatively weak temperature dependence. This is in contrast to the supercurrent which strongly varies with temperature as expected from the exponential dependence of the Josephson coupling on L_T. Nearly identical observations have been made on Al/Au/Al junctions.

In order to further check that the peaks in dI/dV are indeed related to the gap energy we measured another sample with different wire resistance. The critical current of the more resistive sample ($R_N = 34\,\Omega$) was substantially suppressed but the peak voltages remained unaffected as demonstrated by the open symbols in the inset in Fig. 6.11. Earlier experiments on conventional Nb/Nb point contacts [51] have shown a similar suppression of the order parameter at the $n = 1$ peak which was attributed to a reduction of Δ by the relatively high currents which are required to generate the voltage $2\Delta/e$ in low ohmic contacts with $R_N \simeq 20{-}40\Omega$. This leads to deviations from the scaling of the peak voltages, i.e., $V(n = 1)/V(n = 2) \approx 1.6$ instead of 2 in Fig. 6.11. Similar effects are also visible in the data of Ref. [40]. Such a current induced suppression of Δ is also consistent with the value of $\Delta = 163\,\mu$eV extracted from the 2Δ-peaks (see the inset in Fig. 6.11), which is slightly reduced with respect to the bulk value of $186\,\mu$eV.

Another important quantity is the excess current $I_{exc} = I(V) - V/R_N$, i.e. the enhancement of the IV-characteristic above the ohmic straight line. I_{exc} quantifies the integrated proximity correction to dI/dV and saturates at large bias voltages $eV > 2\Delta$, where the Andreev reflection is suppressed. For superconducting point contacts with $E_C \gg \Delta$ the excess current is predicted to be $I_{exc} = (\pi^2/4 - 1)\,\Delta/eR_N \simeq 11\,\mu$A [52]. In the opposite limit of long diffusive junctions with $E_C \ll \Delta$, I_{exc} is suppressed with increasing length as $1/L$ and amounts[53] to $I_{exc} = 0.82\,\Delta/eR_N \cdot \xi^*/L \simeq 2.9\,\mu$A where $\xi^* = \sqrt{\hbar D_S/\Delta}$ and $D_S \simeq 400$ cm^2/s [54]. When integrating the dI/dV curves in Fig. 6.11 we find an asymptotic value of $I_{exc} \simeq 3.5\,\mu$A, which is in acceptable agreement with the theoretical value obtained in the diffusive limit. The excess current is another feature, which is not contained in the RSJ model.

In the case of coherent MAR it is interesting to check for the existence of multiple charge $q^* = e + 2\Delta/V$ transferred during the MAR cycle, which should result in an enhanced shot noise $S_I = 2q^*I$ at low voltages [55, 56, 57]. A first indication for such an effect was seen in NbN based pinhole junctions [41]. Analogous to the dc conductance [21], one may expect also in the noise different types of proximity effects occurring on the length scales L_T and L_Φ. In Fig. 6.12 we present noise data for the same sample as in Figs. 6.9 and 6.11. We indeed find a huge peak in S_V at very low voltages around 3-4 μV $\approx 0.02\,\Delta/e$ which vanishes at elevated temperatures together with the supercurrent.

The noise enhancement appears in the strongly nonlinear part of $I(V)$ (inset in Fig. 6.9). The measured noise is frequency independent between

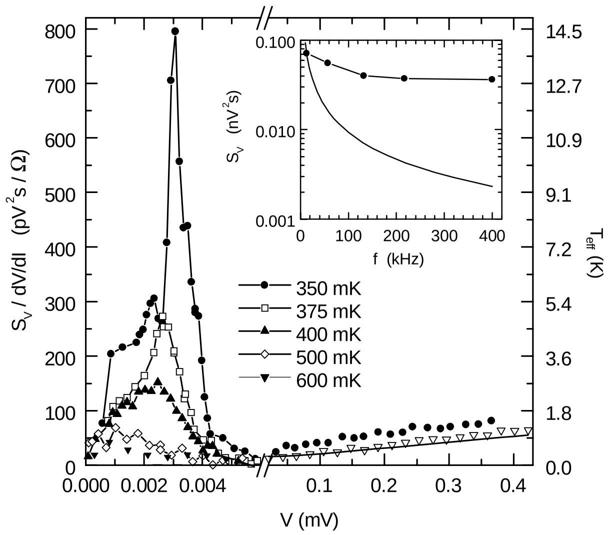

Figure 6.12: Scaled excess noise $S_V/dV/dI$ as a function of voltage for the same device as in Fig. 6.11 with superconducting (•) and normal ($\bigtriangledown$) reservoirs. The resistance per junction is 19.6 Ω in the normal state. The solid line indicates the shot noise of noninteracting electrons in case of normal reservoirs. Note the expanded scale at low V, with data taken at $T = 350$, 375, 400, 500 and 600 mK (from top to bottom). Inset: Amplitude of the low voltage noise peak of a similar sample as a function of frequency. The solid line corresponds to a $1/f$ - dependence.

100 and 400 kHz (see inset in Fig. 6.12). The nonmonotonic dependence of S_V on V is in strong contrast to the 2 μm long Nb/Au sample of Fig. 6.7, which shows no supercurrent at our lowest temperatures and where S_V is monotonically rising with V. At higher voltages we find an enhancement of S_V for superconducting reservoirs (full circles) with respect to normal reservoirs (open triangles). In the voltage regime $V \gtrsim \Delta$ the noise enhancement is most likely caused by heating similar to the Nb/Au case discussed above, where the heating is even more pronounced because of the larger gap of the Nb.

6.4 Discussion

One possible origin of the low voltage noise peak are temporal fluctuations of the critical current as previously observed in grain boundary junctions made from high temperature superconductors [58]. Such critical current fluctuations may be caused by the motion of localized defects close to the junction and should result in a $1/f$ - like frequency dependence of the voltage noise close to I_c as well as of the normal state resistance R_N. The latter would result in a parabolic increase of S_V for $I > I_c$ which is absent in Fig. 6.12. At our typical measuring frequencies $f > 100\,\mathrm{kHz}$ the measured peak height is independent of f (see the inset in Fig. 6.12). For $f < 100\,\mathrm{kHz}$ we observe a small increase of the peak amplitude which is currently not understood, but certainly inconsistent with a $1/f$ law. Hence, $1/f$ noise can be ruled out as the origin of the low voltage noise peak.

Earlier experiments on shunted tunnel junctions have also revealed an increase of the noise at low voltages [59]. This effect has been predicted [60] to arise as a consequence of Johnson-Nyquist noise of the shunt resistor. Fluctuations at high frequencies are mixed down to low frequencies by the highly nonlinear IV characteristics of the junction. Good agreement with the experiment has been found for both the noise rounding of the IV curves and the excess noise. If we calculate the noise according to the RSJ model with the following equation [59];

$$\frac{S_V}{(dV/dI)^2} = \frac{4k_BT}{R_n} + \frac{2eV}{R_n}\left(\frac{I_c}{I}\right)^2 coth\left(\frac{eV}{k_BT}\right) \tag{6.9}$$

and using the measured dI/dV and $I_c(T)$ in the low voltage region for the temperatures shown in Fig. 6.12 we find a peak with an amplitude of 35 $\mathrm{pV^2s/\Omega}$ at 350 mK which is about 20 times smaller than the measured noise peak.

We believe that the noise peak is related to a strongly fluctuating supercurrent at the onset of finite voltage. As discussed already in the context of the IV curves in Fig. 6.9, temporal fluctuations of $|F(x)|$ can be thermally excited at the weak spot in the center of the N wire. These lead to large fluctuations of the supercurrent, and consequently to both large noise and unusually broad IV curves. The minimum in $|F(x)|$ is the specific feature of junctions longer than L_T and is not contained in the treatment of Refs. [55, 56, 57].

The thermally activated fluctuations of the supercurrent have to be distinguished from the fluctuations of the critical current discussed above. The latter correspond to fluctuations of the activation energy with an $1/f$ spectrum, which are negligible at the time scale of μs, where our noise measurements are usually performed.

Independent support of this interpretation is provided by the recent observation of Thomas *et al.* [61], who found a similar thermally activated rounding of the IV characteristics in InAs-based SNS junctions. Their samples are also in the regime $L > L_T$ and the measured activation energy is typically two orders of magnitude smaller than expected from the RSJ model. In our samples, $R(T)$ is also broader than expected from the RSJ model (see the inset in Fig. 6.9). Thomas *et al.* suggest that the rounding of the IV characteristics may be caused by an additional current noise, which is much larger than the Johnson noise of the device. Our work provides direct experimental evidence for such an enhanced noise at the onset of Josephson coupling in "long" ($E_C << \Delta$) SNS contacts.

In contrast to the supercurrent the MAR induced subharmonic gap structure in dI/dV is much less temperature dependent (see Fig. 6.11). This illustrates the already mentioned separation of the two length scales L_T and L_Φ. While the noise peak in Fig.6.12 vanishes for $L_T \lesssim L$ the question remains open, whether there exists also long range effects in the noise gouverned by L_Φ. One possible effect would be the existence of multiple charge quanta $q^* = \Delta/V$ induced by MAR of higher order. These should lead to an enhanced shot noise $S_I = 2q^*I$ at low voltages [55, 56, 57]. In order to check for MAR induced low voltage noise we have to look at higher temperatures where the supercurrent and its corresponding noise peak are suppressed. In Fig. 6.13 we plot the effective charge $q^*/e = S_I/2eI$ vs. $1/V$. At low temperatures $T \lesssim 500$ mK the noise peak in S_V is reflected also in q^*. At higher temperatures $T \gtrsim 500$ mK the peak associated to supercurrent fluctuations vanishes, but we still find a noise signal which rises roughly linear with $1/V$ for $V < 5 - 10\mu V \approx E_C$. At the lowest voltages all curves (dashed lines) seem to merge into a straight line with a slope only slightly lower than $\approx 0.3 \cdot 2\Delta$ as predicted by the theory for the diffusive regime (solid line) [57]. The theory by Naveh and Averin for the MAR noise considers very short junctions with $E_c \gg \Delta$. In our long SNS junctions $E_c \ll \Delta$ is the *smallest* energy scale. To our knowledge, the shot noise has not yet been calculated for this case.

The measured effective charge ranges up to 100 e, which is suprisingly large since the coherence of the MAR cycle is expected to be cut off by inelastic scattering in our samples after a few Andreev reflections. From this point of view, it is already surprising that we find up to four MAR peaks in dI/dV. This raises the question whether phase coherence over $n \times L$ (n is the number of Andreev reflections) is required or only over 1 or 2 $\times$ L. For the regime of our samples, where $L > L_{Thouless}$ it is questionable if phase coherence is required at all to observe MAR. Inelastic scattering would just reset the energy acquired in a AR-cycle to a lower value. The effect is that the conductance peaks will get less sharp in energy, i.e. applied voltage. In contrast for the noise enhancement due to multiple charge transfer a coherent process is required which seems only to be possible in the range where $L_{Thouless} > L$. Although the magnitude and the functional dependence

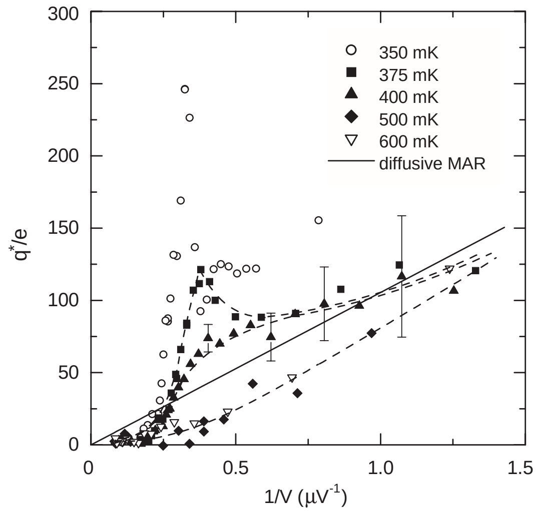

Figure 6.13: Effective multiple charge $q^* = S_I/2eI$ as a function of $1/V$ corresponding to the data in Fig. 6.12. The solid line indicates the theoretical estimate for q^* for the diffusive case [57]. The dashed lines are a guide to the eye. The error bars indicate the uncertainty due to the subtraction of the background noise.

of the low voltage noise in Fig. 6.13 are compatible with the existence of multiple charges, we cannot exclude other possibilities.

6.5 Parallel weak links for I_C control

To clarify the contribution of a fluctuating supercurrent to the noise peak at low bias voltage we designed a sample with two SNS junctions in parallel. Such a geometry is equivalent to a DC-SQUID i.e. a superconducting loop with two Josephson junctions (sec. 2.2.3). The idea of these parallel junctions is to have a means to tune the supercurrent and measure the noise dependence on the coupling strength. In fig. 6.14 the magnetoresistance of a series of 16 Al/Au/Al double junctions is displayed. The Au wires are $1\,\mu m$ long and the area between the junctions is about $37\,\mu\text{m}^2$.

The SEM micrograph in fig. 6.14 shows the double junction fabricated with the shadow technique after removal of the silicon nitride mask. The bright parts are the SiO_2 support layer of the mask. The current is flowing through the parallel wires from the top to the bottom superconducting reservoir. The magnetic field penetrates the area between the junctions perpendicular. The oscillations in the magnetoresistance appear at the onset of superconductivity in the Al reservoirs at a critical field of 9 mT. The analysis of the magnetoresistance shows a periodicity of $40\mu T$ which corresponds to an area of $\Phi_o/40\mu T = 45\mu m^2$. Close to the critical field the oscillation are much more regular than for small fields which is currently not yet understood. The amplitude of the I_c variation is dependent on the homogeneity of the parallel junctions. Only for identical junctions a 100% effect can be expected. In our sample the maximum resistance variation is about 30% of the normal state resistance. Unfortunately it was not possible to stabilize the field of our large 17 tesla magnet on a scale of a few micro tesla. This made it impossible to perform noise measurements exactly at the resistance extrema. An attempt to use a custom-made small superconducting magnet in the direct vicinity to the sample failed until now.

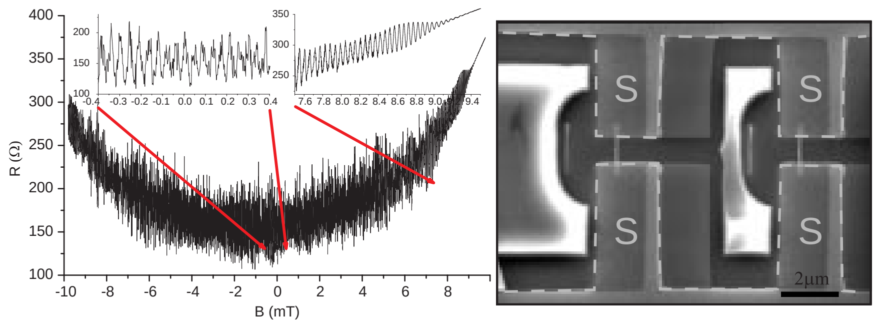

Figure 6.14: Magnetoresistance of a device with two parallel Al/Au/Al junctions shown in the SEM micrograph. The contour of the superconducting layer is accentuated by the dashed line. The area is about $33\,\mu\text{m}^2$ which is in good correspondence with the period of $45\,\mu\text{T}$ of the magnetoresistance.

Chapter 7

S/Ferromagnet/S junctions

When the metal in contact to a superconductor is a ferromagnet, the proximity effect and Andreev reflection are expected to be altered since the spin degenerency is lifted by the presence of an exchange field. Andreev reflection at the SF boundary should be suppressed since the process requires a change of the spinband [62, 63]. The occupation of spin up and spin down states at the Fermi level in the ferromagnet is not equal, leading to a reduced AR probability. Electron-hole coherence is lost on a much shorter length scale than in a normal metal. Electron and hole of opposite spin in a ferromagnet have an energy difference proportional to the exchange field and thus they acquire a phase difference on short distances. The decay length $L_M = \sqrt{\frac{\hbar D}{k_B T_{curie}}}$ of electron-hole coherence is for most ferromagnets only a few nanometers. However some recent experiments suggest that the influence of the superconductor on the ferromagnet is on much larger distances [64, 65]. The wires in these experiments were longer than the phase coherence length, which was demonstrated by the absence of AB oscillations or phase coherent effects in an Andreev interferrometer, but still signatures of proximity effect were observed. Weak localization effects in ferromagnetic films have been reported but also very much doubted [66]. To shed more light on the length scales involved in the proximity effect in a magnetic environment we examined thin (0-5 nm) Co layers between Nb contacts. It is predicted that in the presence of an exchange field the condensation of Cooper pairs with nonvanishing momentum is favoured [67]. The coupling of two superconductors through a magnetic layer could even enhance the condensation if the order parameters in the S layers are just of opposit sign, so called "π - junctions " [68]. It should be mentioned that in a ring containing such a π - junction a spontaneous current will flow which might be experimentally observed. Sputtering technology now permits to grow very fine ferromagnetic layers to study the coupling of the superconductors through the ferromagnet. The influence of magnetic materials on the transition temperature and critical field in SFS multilayers has been investigated in ref [13, 69].

7.1 Oscillation of pairing amplitude in F

Buzdin *et al.* predicted critical current oscillations as a function of the exchange field and the thickness of the ferromagnetic metal in a SFS junction [70]. He showed that the exchange field is responsible for an additional phase shift. As a consequence the superconducting pairing amplitude has a nonmonotoneous decay which is much stronger than for a normal metal and has an oscillatory behaviour. The left graph of fig.7.1 shows I_C as a function of the thickness d_N of the ferromagnetic layer according to [71]

$$I_c R_N = V_0 y \; \frac{|sinh(y)\; cos(y) + cosh(y)\; sin(y)|}{sinh^2(y)\; cos^2(y) + cosh^2(y)\; sin^2(y)} \tag{7.1}$$

where $y = \frac{d_N}{\xi_N}\left(\frac{2I_{exch}}{\pi T_C}\right)^{1/2}$, R_N the normal junction resistance, I_{exch} the exchange energy, $V_0 = \frac{\pi\Delta^2(d_N)}{4eT_C}$ the modulus of the order parameter on the SF boundary. For $T << T_C$ the following expression was derived,

$$I_c R_N = 3.213\frac{\Delta}{e} y \; exp(-y)\; sin(y + \frac{\pi}{4}) \tag{7.2}$$

It can be seen from the above formulas that the period of oscillation and the exponential decay are on the same length scale and depend on the ratio of the exchange field I_{exch} and the critical temperature of the superconductor T_C. When the Curie temperature is not far away from T_C, the critical current I_C is very sensitive to the value of the exchange field, depending itself on temperature (see fig.7.1). For weak ferromagnetic alloys this has been experimentally confirmed [72].

In our experiments we examine the transfer through strong magnetic Co layers ($T_{curie} = 1388\,\mathrm{K}$ for bulk) and set an upper limit to the thickness where a supercurrent is still present. One cannot expect to see the I_C oscillations as a function of temperature since the exchange energy is much higher than the gap energy. The oscillations as a function of thickness of the Co layer might be seen if a series of samples can be measured where the thickness of the ferromagnetic layers is varied by a few Angstroms. In fig.7.2

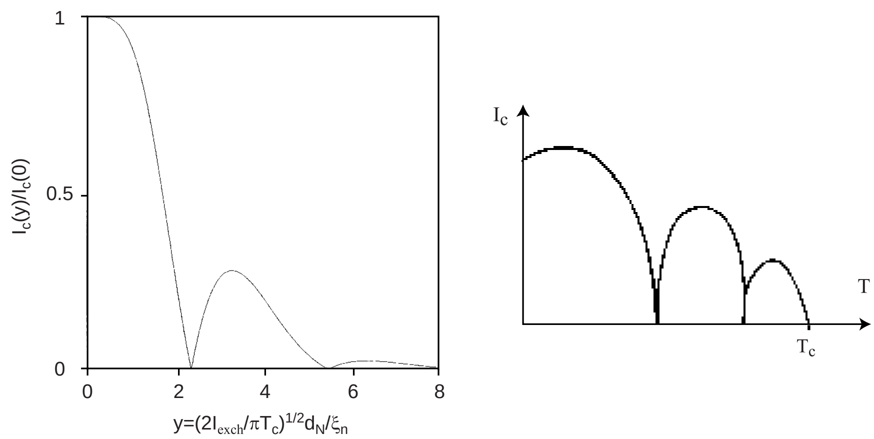

Figure 7.1: Left: $I_C(y)$ dependence [71]. The zeros of I_C correspond to the transition from 0 to π-phase. Right: temperature dependence of a SFS-junction where the Curie temperature is about $2.5T_C$ (schematically)[73].

the critical current according to equation 7.2 and our sample parameters is plotted. The plot has to be considered only quantitatively since the curve change strongly for only minor variations in the sample parameters.

7.2 SFS - sample

Our SFS contacts were realized in a 5 layer Nb/Cu/Co/Cu/Nb system [74]. The Cu was choosen because it is known that very thin ferromagnetic Co layers can be grown on Cu. The fine Cu layer can be considered in first approximation like a superconductor since it will be completely penetrated by the proximity effect from the Nb. Very small contact areas ($\sim 1000\,\mathrm{nm}^2$) were achieved with three angle evaporation through a Si_3N_4 mask. Small junctions are necessary in order to achieve a relatively high junction resistance ($\sim 1\Omega$) and to obtain a good signal to noise ratio in the V(I) measurements. The small contacts have as consequence low critical currents which is favorable to avoid heating effects in the sample. In preliminary experiments on much wider samples heating prevented the determination of I_C as a function of temperature [75]. In fig. 7.3 a SEM micrograph shows the junction area from an oblique point of view. The Nb fingers at both ends of the junction lead to large contact areas where current and voltage probes are bonded. When the Nb is superconducting the junction is connected in a four probe configuration. From the front side (with respect to

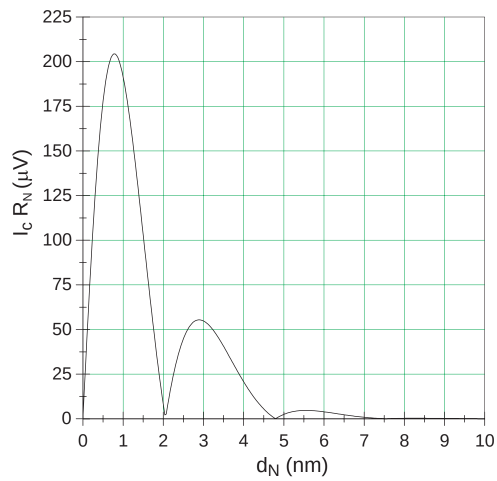

Figure 7.2: $I_C R_N$ product as a function of magnetic layer thickness for $T << T_C$ according to eq.7.2. The function starts at zero because $R_N = 0$ for $d_N = 0$. The parameters use for the plot are: $I_{exch} = 1338\,\mathrm{K}$, $d_N = 5\,\mathrm{nm}$, $\xi_N = \sqrt{\hbar D/2\pi k_B T_C} = 9\,\mathrm{nm}$, $D = 5{*}10^{-4}\,\mathrm{m}^2\mathrm{s}$, $T_C = 8\mathrm{K}$.

fig.7.3) the first Nb layer was deposited. The Cu/Co/Cu was evaporated from the left to cover also the edge of the first S layer. This was necessary to avoid a direct SS short circuit in the overlap region. In a last step, from the backside, the second Nb layer is deposited. The base pressure in the evaporation chamber was $3-4\times10^{-11}$ mbar. Nb and Cu were evaporated at 1 Å/s, Co at 0.1 Å/s. Different samples were prepared with 0,1 and 5 nm Co layers. The V(I) measurements were done with a DC current source and a nanovoltmeter. This setup allows faster measurements compared to the lock-in techique. All samples showed a Josephson current. To test the homogeneity of the magnetic layer we were loocking at the magnetic field dependence of the critical current. Only the 5 nm Co sample showed the expected Fraunhofer pattern for a homogeneous Josephson junction (see sec. 2.2.3) and will be further discussed. Fig.7.4 shows R(T) and V(I). The transition of the Nb is at 8.5 K, which is slightly suppressed with respect to the bulk value of 9.25 K. The additional two steps in R(T) might stem from different regions of the sample. Due to the angle evaporation there are areas of the leads which are either S, SF or a SFS multilayers. It is very probable that this affects the transition temperature. The last step is magnified in the inset and represents the transition of the SFS junction from normal resistance to Josephson current. The resistance drop corresponds to the slope of 1.36 Ω in the V(I) characteristic. The V(I) behavior shows a resistiveless current until a critical value where the curve aproaches rapidly the ohmic linear behavior. Note that here the high current behavior of V(I) (not shown) extrapolates through zero and has no excess current as the long

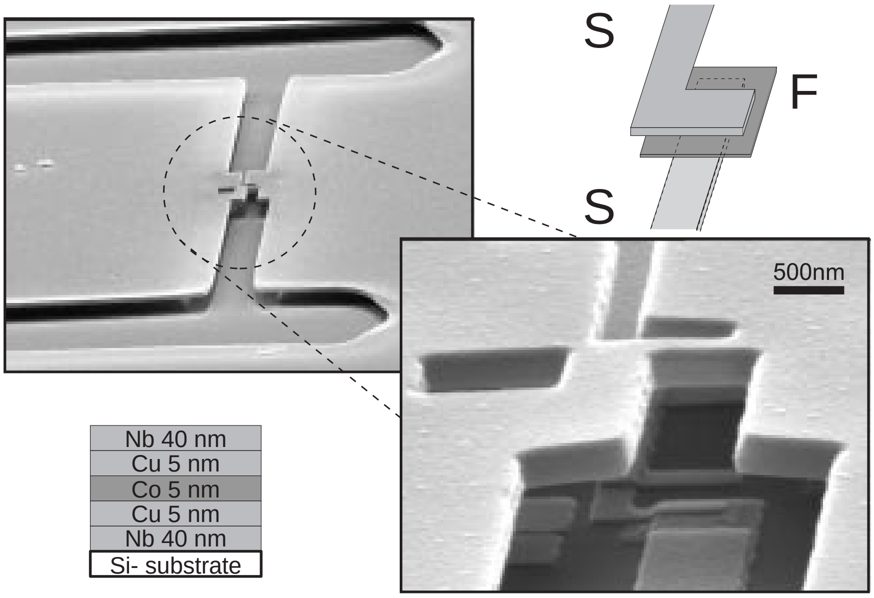

Figure 7.3: SFS junction realized in a Nb/Cu/Co/Cu/Nb multilayer. Very small contact area was achieved by evaporating the layers from three different angles through a Si_3N_4-mask. This technique produces also artefact structures, however they are not in contact to the junction. The schematic on top right shows the actual junction geometry.

SNS junctions of the previous chapter. Critical current as a function of temperature and magnetic field is displayed in fig.7.5. The critical current of $8\,\mu$A is in reasonable agreement with the exponential decay of the supercurrent according to eq.7.2. The exponential term gives a maximum critical current of $7.7\,\mu$A, however the oscillating term causes strong variations for minor changes in sample parameters. In this case the sin is 0.23 and the resulting critical current is $1.8\,\mu$A. The strong damping of I_C by the magnetic layer can be seen when compared to the result of Ambegaokar-Baratoff (AB) where $I_C = \pi\Delta(0)/2e\mathrm{R}_N = 1.5\,\mathrm{mA}$. It was not possible to simulate the temperature dependence with the Ambegaokar-Baratoff formula 2.20 even if the reduced maximum I_C was considered. The AB result is decreasing more slowly up to higher temperatures and hits then the x-axis at a linear slope.

For the magnetic field dependence of I_C a field parallel to the layers and hence perpendicular to the SFS-junction was applied. The critical current shows an oscillatory behaviour which is independent of temperature.

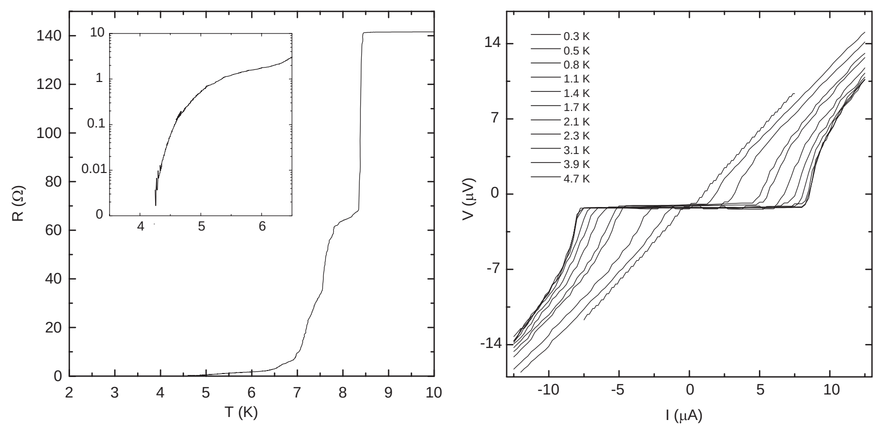

Figure 7.4: Left: R(T) of a SFS junction with 5 nm Co layer. The first three steps in R(T) are most probable from sample areas with different layering of S and F materials. The resistance drop over the junction is magnified in the inset. Right: V(I) characteristic as a function of temperature.

This proves the uniformity of the junction layer. The Josephson current goes to zero as the superconductivity in the Nb is quenched at 5 T. The period in R(B) corresponds to an area perpendicular to the magnetic field of $0.007\,\mu\mathrm{m}^2$ which compares very well to the junction geometry of about $500\,\mathrm{nm}\times 15\,\mathrm{nm}$. In order to check if the Co is magnetic for such a fine layer, we were looking for magnetization effects. If the Co layer is not saturated it should be possible to enhance the ordering of the spins by applying a strong field. When the external field is removed the intrinsic field of the magnetized layer should result in a shift of the Fraunhofer (FH) pattern at low fields. In fig.7.6 we first recorded the FH pattern at low fields and then magnetized the Co film at 8 T. The measurement down from 1.5 T shows a shift of the oscillations to higher fields as expected. However, at about 0.5 T it approaches the data from prior to magnetization. This is not well understood but it might be a time dependent relaxation effect since the measurement takes about 1.5 h per Tesla. In order to investigate the critical current behaviour as a function of thickness of the ferromagnetic layer we are currently measuring samples with 3.5 nm and 6.5 nm Co layer.

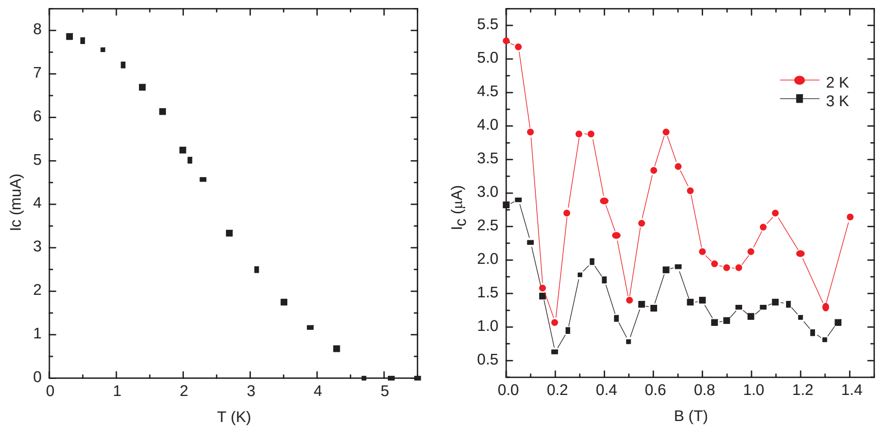

Figure 7.5: Critical current as a function of temperature and magnetic field. The maximum critical current is of the theoretically expected order. No I_C reversal or oscillation can be seen since the exchange field is constant. Right: The observation of a Fraunhofer pattern confirms the homogeneity of the Co junction layer.

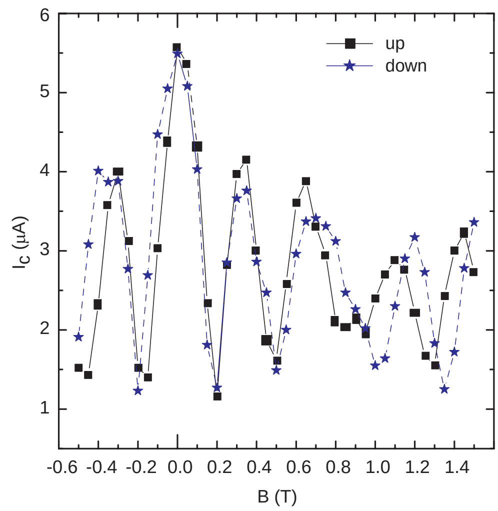

Figure 7.6: Fraunhofer oscillations for two magnetic field ramps. First from -0.5 to $1.5\,\mathrm{T}$. Then magnetisation of the Co at 8T and subsequently a ramp down from 1.5T. First the pattern is shifted by $100\,\mathrm{mT}$ but approaches the initial curve at half way to zero field.

Chapter 8

Summary

In this thesis a new fabrication technique has been developed which proved to be especially suited for structuring on a submicron scale. Clean superconducting wires and multilayer junctions have been prepared. The measurement setup has been equipped with a HF-filtering that effectively suppresses external high frequency interference and made it possible to observe mesoscopic effects at all. By means of noise measurements we have shown that multiple Andreev reflections in a normal metal wire sandwiched between two superconductors lead to substantial electron heating in the wire. The strength of this heating effect depends on the size of the gap in the superconductors. For Nb with a large gap the effective electron temperature rises already for small currents up to several K, which leads to a suppression of coherent multiple Andreev reflection. For the smaller gap superconductor Al the heating is less pronounced and subharmonic gap structure becomes visible. Conductance enhancement by MAR has been seen in gold and copper wires up to the fourth order process, which has not been investigated in such a system before. With the onset of a proximity induced supercurrent through the normal wire a sharp noise peak appears at low voltages, which we attribute to thermally induced fluctuations of the supercurrent. When the supercurrent is suppressed at moderately elevated temperatures another contribution to the noise remains at low voltages, which indicates the existence of a long range coherence effect in the noise. The interpretation of the noise enhancement in terms of multiple charge transfer could not be confirmed unequivocally. Further effort has to be made to separate the Josephson current from the coherent MAR. It would be interesting to see if they are both governed by the same energy scale or if they could be separated in temperature or magnetic field. The influence of the effects based on the Thouless energy are not clearly distinguishable since they are covered by the larger energy kT. In collaboration with C. Sürgers, University of Karlsruhe, we have fabricated mesoscopic Nb/Co/Nb junctions with a contact area of $200\,\mathrm{nm}\times 500\,\mathrm{nm}$. This is the first demonstration of the dc Josephson effect through a homogeneous strong ferromagnet. The measured critical current is in agreement with the strong exponential decay of the Josephson current due to the exchange field in the magnetic layer. To investigate the predicted critical current oscillations as a function of magnetic layer thickness a new measurement series is in progress.

Appendix A

Process details

A.1 Wafer cleaning

The wafers we received from the IMT Neuchatel were clean in the sense of the high industrial standards. In this regard no pre-process cleaning was required. During the process two sorts of cleaning were used.
– A reactive oxygen ion plasma to remove the carbon layer which is always on the sample after SEM inspection.
– A sequence of ultrasonic bath of aceton, ethanol and DI water to remove all organic materials like PMMA.
The ultrasonic is especially useful to remove charged particles from the surface, like silicon grains after cleaving the wafer.

A.2 BHF

The buffered hydro fluorid acid was used to increase the selective etching of SiO_2 and Si_3N_4. For Si_3N_4 no measurable etchrate was observed. With the following recipe the etchrate for SiO_2 was $1\mu m/20min$:
28 ml HF (40%)
107 ml H_2O
113 g NH_4F

A.3 Bonding

When bonding the sample, special care has to be taken that the bondwires don't touch the top layer of the mask that is surrounding the structure.

Otherwise the sample can be short circuit or grounded. To prevent this a high loop from first to the second bond is necessary. To ensure that the bondwire is leaving the contact pad in a steep angle it is sometimes necessary to bend the bondwire with a fine needle.

A.4 Mechanical lift off

The most effective method to remove the Si_3N_4 evaporation mask from the substrate was to lift it together with a layer of PMMA. A droplet of very diluted PMMA (2%) is put on top of the sample. To improve the wetting below the mask the sample is fixed on a carrier which is connected to an ultrasonic bath. When the droplet has dried this is repeated for four more times. Then highly concentrated PMMA (9%) is added on top and left to dry for at least 3 hours. The PMMA layer can be grabbed with a tweezer and lifted off together with the nitride mask sticking to it.

A.5 Quality control

The major rule is; the less manipulation the less contamination. It is sufficient to check the sample quality with a SEM after the transfer of the e-beam pattern to the Si_3N_4 is done by RIE. Here the structures can be inspected and the distances measured that are necessary for the angle evaporation. After SEM inspection it is crucial to clean the sample with an oxygen plasma. Otherwise a fine layer of amorphous carbon, covering the step between the mask and the etchpit, will remain after the wet etching of the SiO_2 spacer layer. A second and final inspection is done after the wire bonding.

Bibliography

[1] P. Dubos, P. Charlat, Th. Crozes, P. Paniez and B. Pannetier, cond-mat/9909053 (1999).

[2] R. Landauer, J. Res. Dev. **1**, 233 (1957).

[3] Y. Imry, R. Landauer, Rev. Mod. Phys. **71**, S307 (1999).

[4] V.A. Khlus, Zh. Eksp. Teor. Fiz. **93**, 513 (1987); M. Bttiker, Phys. Rev. Lett. **65**, 2901 (1990).

[5] W. Schottky, Ann. Phys. **57**, 541 (1918).

[6] M.B. Johnson, Phys. Rev. **29**,367 (1927); H.Nyquist, ibid **32**, 110 (1928).

[7] O.N. Dorokhov, Solid State Commun. **51, 381** (1984).

[8] Y. Naveh, D.V. Averin and K.K. Likarev, Phys. Rev. B **58**, 15 371(1998).

[9] Th. Martin and R. Landauer, Phys. Rev. B **45**, 1742 (1992).

[10] F.N. Hooge, IEEE Trans. Electron Devices **41**, 1926 (1994).

[11] A. Bezryadin, C.N. Lau, and M.Tinkham, cond-mat/0003198 (2000).

[12] C.T. Black, D.C. Ralph, and M. Tinkham, Phys. Rev. Lett. **76**, 688 (1996); K.A. Matveev and A.I. Larkin, Phys. Rev. Lett. **78** 3749 (1997).

[13] T. Müghe et al., Phys. Rev. B **57**, 5071 (1998).

[14] T.P. Orlando, J.E. Mooij, Lin Tian, C.H. van der Wal, L.S. Levitov, Seth Lloyd, J.J. Mazo, Phys. Rev. B **60**, 15398 (1999).

[15] A. A. Andreev, JETP **19**, 1228 (1964).

[16] G. E. Blonder, M. Tinkham, and T. M. Klapwijk, Phys. Rev. B **25**, 4515 (1982).

[17] B.D. Josephson, Phys. Lett. **1** 251 (1962).

[18] V. Ambegaokar and B. I. Halperin, Phys. Rev. Lett. **22**, 1364 (1969).

[19] W. Belzig, C. Bruder and G. Schön, Phys. Rev. B **54**, 9443 (1996).

[20] P. Charlat, H. Courtois, Ph. Gandit, D. Mailly, A.F. Volkov and B. Pannetier, Phys. Rev. Lett. **77**, 4950 (1996).

[21] H. Courtois, Ph. Gandit, D. Mailly and B. Pannetier, Phys. Rev. Lett. **76**, 130 (1996).

[22] A.F. Morpurgo, B.J. van Wees, T.M. Klapvijk and G. Borghs, Phys. Rev. Lett. **79**, 4010 (1997).

[23] N. Argaman, cond-mat/9903069 (1999).

[24] J.J.A. Baselmans,A.F. Morpurgo, B.J. van Wees, T.M. Klapwijk, Nature **397**,43 (1999).

[25] F.K. Wilhelm, G. Schön and A.D. Zaikin, cond-mat/9803091 (1998).

[26] Y. Harada et al, Appl. Phys. Lett. **65** 636 (1994).

[27] G. J. Dolan, Appl. Phys. Lett. **31** 337 (1977).

[28] M. Henny, PhD thesis [1998].

[29] H. S. J. van der Zant,H. a. Rijken, and J. E. Mooij, J. Low Temp. Phys. **79** 289 (1990).

[30] R. E. Howard, Appl. Phys. Lett. **33** 1034 (1978).

[31] A.B. Zorin, Rev. Sci. Instrum. **66**, 4296 (1995).

[32] B. van Wees, Physics World **11** (1996).

[33] B.J. van Wees, B.J.P. de Vries, P. Magne and T.M. Klapwijk, Phys. Rev. Lett. **69**, 510 (1992).

[34] K. E. Nagaev, Phys. Lett. A **169**, 103 (1992).

[35] H. Pothier *et al.*, Phys. Rev. Lett. **79**, 3490 (1997).

[36] A. Steinbach, J. M. Martinis, and M. H. Devoret, Phys. Rev. Lett. **76**, 3806 (1996).

[37] R. J. Schoelkopf *et al.*, Phys. Rev. Lett. **78**, 3370 (1997).

[38] M. Henny, S. Oberholzer, C. Strunk, and C. Schönenberger, Phys. Rev. B **59**, 2871 (1999).

[39] P. E. Gregers-Hansen *et al.*, Phys. Rev. Lett. **31**, 524 (1973); T. M. Klapwijk, G. E. Blonder, and M. Tinkham, Physica **109&110B**, 1657 (1982); W. M. van Huffelen *et al.*, Phys. Rev. B **47**, 5170 (1993); A. W. Kleinsasser *et al.*, Phys. Rev. Lett. **72**, 1738 (1994); E. Scheer *et al.*, Phys. Rev. Lett. **78**, 3535 (1997).

[40] J. Kutchinsky *et al.*, Phys. Rev. Lett. **78**, 931 (1997).

[41] P. Dieleman, H.G. Bukkems, T.M. Klapwijk, M. Schicke, and K.H. Gundach, Phys. Rev. Lett. **79**, 3486 (1997).

[42] X. Jehl *et al.*, Phys. Rev. Lett. **83**, 1660 (1999).

[43] H. Courtois, Ph. Gandit, and B. Pannetier, Phys. Rev. B **52**, 1162 (1995); F. K. Wilhelm, A. D. Zaikin, and G. Schön, J. Low Temp. Phys. **106**, 305 (1997).

[44] B.L. Altshuler and Aronov, Pis'ma Zh. Eksp. Teo. Fiz. **33**, 515 (1981) [JETP lett. **33**, 499 (1981)].

[45] G. Bergmann, Phys. Rep. **107**, 1 (1984).

[46] G. Bergmann, Solid State Comm. **42**, 815 (1982).

[47] V. Chandrasekhar, P. Santhanam and D.E. Prober, Phys. Rev. B **44**, 11 203 (1991).

[48] M. Henny *et al.*, Appl. Phys. Lett. **71**, 773 (1997).

[49] F. C. Wellstood, C. Urbina and J. Clarke, Phys. Rev. B **49**, 5942 (1994).

[50] C.M. Falco, W.H. Parker, and S.E. Trullinger, Phys. Rev. B **10**, 1865 (1974).

[51] K. Flensberg and J. Bindslev Hansen, Phys. Rev. B **40**, 8693 (1989).

[52] A. Bardas and D. V. Averin, Phys. Rev. B **56**, R8518 (1997).

[53] A. F. Volkov, A. V. Zaitev and T. M. Klapwijk, Physica C **210**, 21 (1993).

[54] The coherence length on the superconducting side enters because of the modulation of the order parameter of the superconductor at the NS interface.

[55] D. Averin and H. Imam, Phys. Rev. Lett. **76**, 3814 (1996).

[56] J. C. Cuevas, A. Martín-Rodero, and A. Levy-Yeyati, Phys. Rev. Lett. **82**, 4086 (1999).

[57] Y. Naveh and D. V. Averin, *ibid.* p. 4090.

[58] M. Kawasaki, P. Chaudhari and A. Gupta, Phys. Rev. Lett. **68**, 1065 (1992); A. Marx *et al.*, Phys. Rev. B **51**, 6735 (1995).

[59] C. M. Falco *et al.*, Phys. Rev. B **10**, 1865 (1974); R. H. Koch, D. J. Van Harlingen, and J. Clarke, Phys. Rev. B **26**, 74 (1982).

[60] K. K. Likharev and V. K. Semenov, JETP Lett. **15**, 442 (1972); R. H. Koch, D. J. Van Harlingen, and J. Clarke, Phys. Rev. Lett. **45**, 2132 (1980).

[61] M. Thomas *et al.*, Phys. Rev. B **58**, 11676 (1998).

[62] M.J.M. de Jong and C.W.J. Beenakker, Phys. Rev. Lett. **74**,1657 (1995).

[63] S.K. Upadhyay, A. Palanisami, R.N. Louie, R.A. Buhrman, Phys. Rev. Lett. **81**, 3247 (1998).

[64] M. Giroud, H. Courtois, K. Hasselbach, D. Mailly and B. Pannetier, Phys. Rev. B **58**, R11872 (1998).

[65] V.T. Petrashov, I.A. Sosnin, I. Cox, A. Parsons, C. Troadec, Phys. Rev. Lett. **83**, 3281 (1999).

[66] M.D. Lawrence and N. Giordano, J. Phys.: Cond. Matter **8** L563 (1996).

[67] P. Fulde, R.A. Ferrell, Phys. Rev. **135(3A)** 550 (1964); A.I. Larkin, Yu. N. Ovchinnikov, JETP **20(3)** 762 (1965).

[68] A.V. Andreev, A.I. Buzdin, and R.M. Osgood, Phys. Rev. B **43**, 10124 (1991).

[69] C. Strunk, Ph.D. thesis (1992).

[70] A.I. Buzdin, L.N. Bulaevskii and S.V. Panyukov JETP Lett. **3**5, No.4, 178 (1982).

[71] A.I. Buzdin, M.Yu. Kupriyanov, B. Vujicic, to be published in Physica C.

[72] A.V. Veretennikov, V.V. Ryazanov, V.A. Oboznov, A.Y. Rusanov, V.A. Larkin, Jan Aarts, Proceedings to the LT conference 1999, submitted to Physica B.

[73] L.N. Bulaevskii, A.I. Buzin, S.V. Panjukov, Solid State Comm. **44**, 539 (1982).

[74] The deposition of the Nb/Cu/Co multilayers was done by C. Sürgers, Universität Karlsruhe.

[75] C. Hauschel, Diploma work (1999).

List of publications

Publications in journals and proceedings:

- *Contacting single template synthesized nanowires for electric measurements*, A. Bachtold, C. Terrier, M. Krüger, M. Henny, T. Hoss, C. Strunk, R. Huber, H. Birk, U. Staufer and C. Schönenberger, Microelectronic Engineering **41/42**, 571-574 (1998).
- *Nonorganic evaporation mask for superconducting nanodevices*, T. Hoss, C. Strunk and C. Schönenberger, Microelectronic Engineering **46** 1-4 (1999) pp. 149-152
- *Multiple Andreev Reflection and Giant Exess Noise in Diffusive Superconductor/ Normal-Metal/ Superconductor Junctions*, T. Hoss, C. Strunk, T. Nussbaumer, R. Huber, U. Staufer, and C. Schönenberger, submitted to Physical Review B (status: to be published)
- *Andreev reflection and excess noise in mesoscopic SNS junctions*, C. Strunk, T. Hoss, T. Nussbaumer, and C. Schönenberger, Proceedings of Rencontres Moriond, Quantum Physics at Mesoscopic Scale, Les Arcs, France, January 1999

Talks:

- *Multiple Andreev Reflektion in diffusiven SNS Kontakten*, Frühjahrstagung der Deutschen Physikalischen Gesellschaft, Münster, 22.-26. march 1999
- *Multiple Andreev Reflection and excess noise in diffusive SNS junctions*, Quantum Mesoscopic Phenomena and Mesoscopic Devices in Microelectronics, Ankara,Turkey on 13-25 June 1999.

Poster contributions:

- *Fabrication of Metallic Nanoconstrictions in Silicon*, Workshop des SFB 513, Konstanz,15.-18. July 97

- *Diffusive SNS junctions*, "Nanostructures at Surfaces and Interfaces", Discussion Meeting Ascona, 19.-24. April 98
- *Nonorganic evaporation mask for superconducting nanodevices*, International Conference of Micro- and Nanoengineering 98 in Leuven, Belgium, 22.-24.9.98.
- *Noise and conductance measurements in diffusive SNS-junctions*, Nano Forum CH-US 99, ETH Zürich, 20-22 September 1999
- *Transport and excess noise measurements in mesoscopic SNS and SFS junctions*, EPS-CMD18 conference in Montreux, Switzerland.11-16 February 2000.

Curriculum Vitae

Tilman Hoss

16. 1. 1972	Geboren in Freiburg im Breisgau
1978 - 1982	Besuch der Grundschule in Herrischried
1983 - 1991	Besuch des Scheffel-Gymnasiums Bad Säckingens Abschluss mit allgemeiner Hochschulreife
1991 - 1997	Studium an der Universität Basel in den Fächern Physik, Mathematik und französischer Literatur
1993	Vordiplom in Physik und Mathematik
1995	Wahlfachprüfung in französischer Literatur des 18. Jhdts
1996	Diplom in Physik
1997	Diplomarbeit in der Gruppe von Prof. Dr. Ch. Schönenberger, Thema: "Herstellung von metallischen Punktkontakten in dünnen Siliziummembranen"
1997	Beginn der Dissertation unter der Leitung von Prof. Dr. C. Schönenberger zum Thema "Electrical Transport and Noise in Mesoscopic SNS/SFS-junctions" Assistent zur Vorlesung "Kondensierte Materie" und dem Anfängerpraktikum
8. 6. 2000	Mündliche Doktorprüfung

Dozentinnen und Dozenten meiner wissenschaftlichen Ausbildung:

G. Backenstoss, C. Bruder, H. Burkhart, N. A'Campo. J. Fünfschilling, H. C. Im Hof, D. Masser, H. Rudin, C. Schönenberger, I. Sick, C. Strunk, L. Tauscher, H. Thomas, D. Trautmann, R. Wagner, I. Zschokke-Gränacher

Danksagung

Während meiner Doktorarbeit habe ich von vielen Personen grosse Unterstützung erhalten. Besonders geschätzt habe ich die enge Zusammenarbeit mit Christoph Strunk, der alle Experimente mit begleitet hat. Mein Professor, Christian Schönenberger, hat mich bei der Planung und Interpretation immer sehr stark unterstützt und er war mir eine gute Schule für klar strukturierte Präsentation der Ergebnisse. Er war für mich nicht nur Chef sondern auch Arbeitskollege in einer Gruppe mit freundschaftlicher Zusammenarbeit. Ich möchte allen Gruppenmitgliedern für diese gegenseitige Hilfe danken. Den Postdoktoranden; Dinco Babic, Holger Birk, Richard Huber, Madi Iqbal, Thomas Nussbaumer, Urs Staufer, sowie den Doktoranden; Adrian Bachthold, Mark Buitelaar, Francois Dewarrat, Matthias Henny, Michael Krüger, Stefan Oberholzer und Christope Terrier. Ich möchte mich auch bei Christoph Sürgers für die Unterstützung bei der Probenherstellung bedanken und es war mir eine Freude mit ihm die letzten Experimente durchzuführen. Urs Staufer hat grossen Anteil an meiner Arbeit, da er nicht nur die Proben Substrate geliefert hat sonder mich auch in die Mikrofabrikationstechniken eingewiesen hat. All die Modifikationen an den Messapparaturen wären ohne die mechanische Werkstatt, unter Leitung von Herrn Cattin, nicht möglich gewesen. Herrn Roth gebührt besondere Anerkennung, da er unsere dringenden Aufträge oft mit Vorzug behandelt hat und die Versorgung mit flüssigem Helium sicherstellte. Dass ich solch schöne Doktorandenjahre verbringen konnte, ist natürlich auch meiner Familie und meinen Freunden zu verdanken. Sie haben mir eine abwechslungsreiche und erfüllte Zeit bereitet und haben mir über gelegentliche Durststrecken hinweg geholfen.

Diese Arbeit wurde vom Schweizerischen Nationalfond unterstützt.